Technobius Physics

A peer-reviewed open-access journal

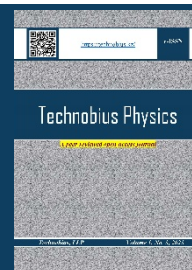| **Contacts:**	Website:	https://technobius.kz/
	E-mail:	technobiusphysics@gmail.com

CONTENTS

Article

Exploring the phase composition and crystal structure of potassium-doped copper sulfide

Saira Sakhabayeva[1,*], Azat Nurkasimov[2], Murat Kasymzhanov[2], Zhanat Baigazinov[2]

[1]Department of Physics, School of Science and Humanities, Nazarbayev University, Astana, Kazakhstan
[2]The Nuclear Technology Park, JSC, Kurchatov, Kazakhstan
*Correspondence: saira.sakhabayeva@nu.edu.kz

Abstract. This study investigates the phase composition, crystal structure, and phase transitions of potassium-substituted copper sulfide ($K_x Cu_{1.97-x}S$), focusing on the effects of potassium doping on the material's properties. Using X-ray diffraction analysis, we identified the structural characteristics of potassium-doped variants, confirming their retention of the monoclinic chalcocite structure (P21/c) with slight modifications in lattice parameters. The incorporation of potassium ions resulted in observable changes in the unit cell dimensions, suggesting enhanced ionic interactions and potential impacts on electronic conductivity. The thermoelectric coefficient, electron conductivity, and thermoelectric power were also examined, revealing that potassium doping could stabilize certain phases under varying temperature conditions. This work provides valuable insights into the structure-property relationships in copper sulfides, highlighting the potential for tailored materials in thermoelectric applications and other advanced technologies. Future studies will explore the implications of these findings for optimizing the performance of potassium-doped copper sulfides in practical applications.

Keywords: copper sulfide, potassium doping, phase composition, crystal structure, thermoelectric power, thermoelectric coefficient, electro-conductivity.

1. Introduction

Copper sulfides, particularly the chalcocite (Cu_2S) phase, have garnered significant attention in materials science due to their unique electronic, thermal, and optical properties. These materials play a crucial role in various applications, including thermoelectric devices, photovoltaics, and batteries. The ability to tailor their properties through ionic substitution offers an exciting avenue for enhancing performance and expanding their usability.

Incorporating potassium (K^+) into copper sulfide systems is of particular interest, as it can alter the crystal structure, phase stability, and electrical characteristics of the material. Potassium substitution may modify the lattice parameters, introduce defects, and enhance charge carrier mobility, thereby influencing the material's overall behavior. Previous studies have indicated that alkali metal substitutions can significantly impact the physical properties of chalcocite and its related phases, making them potential candidates for improved thermoelectric performance.

The study of the phase composition, crystal structure, and phase transitions in copper sulfide substituted with potassium involves analyzing the behavior of the material when potassium is introduced into the crystal lattice. The research suggests that potassium may be dissolved in the voids of the copper sulfide crystal lattice, leading to various phases of copper sulfide without distinct potassium-containing phases [1]. The crystal structure and phase transitions in copper sulfide have been the subject of investigation, including the low-temperature behavior and phase transition of tetragonal copper sulfide ($Cu2S$) to an orthorhombic structure [2]. The presence of surface sulfur in copper sulfide has also been studied, particularly in the context of electrocatalytic applications [3].

The research provides insights into the structural characteristics and behavior of copper sulfide and its derivatives, contributing to the understanding of their properties and potential applications.

Potassium-doped copper sulfide is a versatile material with potential applications across various fields. As a cathode material for potassium-ion batteries (PIBs), it enhances charge-discharge efficiency and cycling stability by accommodating potassium ions within its crystal structure, making it suitable for next-generation battery technologies [4]. Its high conductivity and electrochemical stability also make it ideal for supercapacitors, providing high energy density and rapid charge/discharge capabilities. In photovoltaics, its semiconductor properties allow for efficient light absorption and charge carrier generation, improving the efficiency of thin-film solar cells [5]. Additionally, its thermoelectric properties, enhanced through potassium doping, make it useful in thermoelectric generators and coolers, contributing to energy efficiency and waste heat recovery [6]. Potassium-doped copper sulfide can also serve as a catalyst in chemical reactions, such as hydrogen evolution and CO_2 reduction, due to its unique electronic structure. Furthermore, its electrical properties make it suitable for sensor applications, including gas sensors and biosensors, where its sensitivity to environmental changes is advantageous for detecting specific gases or biological markers [7].

This study aims to investigate the phase composition, crystal structure, and phase transitions of potassium-substituted copper sulfide. By analyzing the structural modifications induced by potassium doping, we seek to elucidate the relationship between composition and properties, providing a comprehensive understanding of how such substitutions can enhance the functionality of copper sulfides. Through this work, we aim to contribute to the ongoing efforts to develop advanced materials for energy conversion and storage applications.

2. Methods

Potassium-substituted copper sulfides were synthesized using a sparkling method. In this approach, copper(I) sulfide (Cu_2S) and potassium sulfide (K_2S) were mixed in stoichiometric ratios and subjected to a high-energy ball milling process to ensure thorough mixing and activation of the reactants. The mixture was then placed in a quartz ampoule under an inert atmosphere to prevent oxidation. The ampoule was heated to 600°C for 12 hours, followed by a controlled cooling process to room temperature. This method ensures a homogenous distribution of potassium within the copper sulfide matrix, enhancing the material's structural and functional properties. The synthesized materials were characterized using various techniques: X-ray Diffraction (XRD) with a Bruker D8 Advance diffractometer to determine phase composition and crystal structure; The Ulvac ZEM-3 setup was used for the simultaneous measurement of the temperature dependence of electrical conductivity and thermoelectric coefficient.

The statistical data analysis methods were carefully applied to ensure the reliability and accuracy of the results. The following key approaches were used.

Each sample underwent at least three independent measurements for each parameter (e.g., phase composition, electrical conductivity, and thermoelectric coefficient). This approach helped to obtain more objective results by minimizing the impact of random errors.

The average value was calculated from the collected data, representing the central tendency for each measured property. The standard deviation was calculated to assess the dispersion of the data around the mean, indicating the degree of variability in the measurements. Confidence intervals with a significance level of 95% ($p < 0.05$) were also determined. The confidence interval reflected the range within which the true value of the measured parameter was likely to fall, providing a measure of the data's precision and reliability.

To compare results between different sample series (e.g., $K_{0.01}Cu_{1.96}S$, $K_{0.02}Cu_{1.95}S$, and $K_{0.03}Cu_{1.94}S$), Student's t-test for independent samples was applied. This test determined whether the differences between the groups were statistically significant. If the p-value was below 0.05, the differences were considered statistically significant.

To investigate the relationships between measured properties, such as electrical conductivity and thermoelectric coefficient, Pearson's correlation coefficient was used. This method assessed the strength and direction of the relationship between two variables, providing insights into potential dependencies between material properties.

All results were presented graphically, with error bars indicating the standard deviation and confidence intervals. This visual representation enhanced the clarity of the data and allowed for an easier comparison of trends between different sample groups.

3. Results and Discussion

Crystal Structure of Potassium-doped Copper Sulfide ($K_{0,01}Cu_{1,96}S$, $K_{0,02}Cu_{1,95}S$ and $K_{0,03}Cu_{1,94}S$)

The crystal structure of potassium-doped copper sulfide ($K_xCu_{1.97-x}S$) is a key factor influencing its physical and chemical properties. This structure can vary depending on the concentration of potassium, which can lead to significant changes in the lattice parameters and symmetry.

The XRD pattern of the sample at Figure 1 labeled "$K_{0.03}Cu_{1.94}$" provides essential insights into its crystalline structure and phase composition. The pattern exhibits several sharp peaks at specific 2-theta angles, with prominent peaks around 35°, 38°, and 58-62°, indicating well-defined crystallographic planes.

The intensity of these peaks exceeds 3000 arbitrary units (a.u.) for the highest peaks, reflecting a high degree of crystallinity. By comparing these peak positions with standard reference patterns, the phases present can be identified, likely corresponding to the monoclinic structure of chalcocite (Cu_2S) with modifications due to potassium incorporation on Figure 1a.
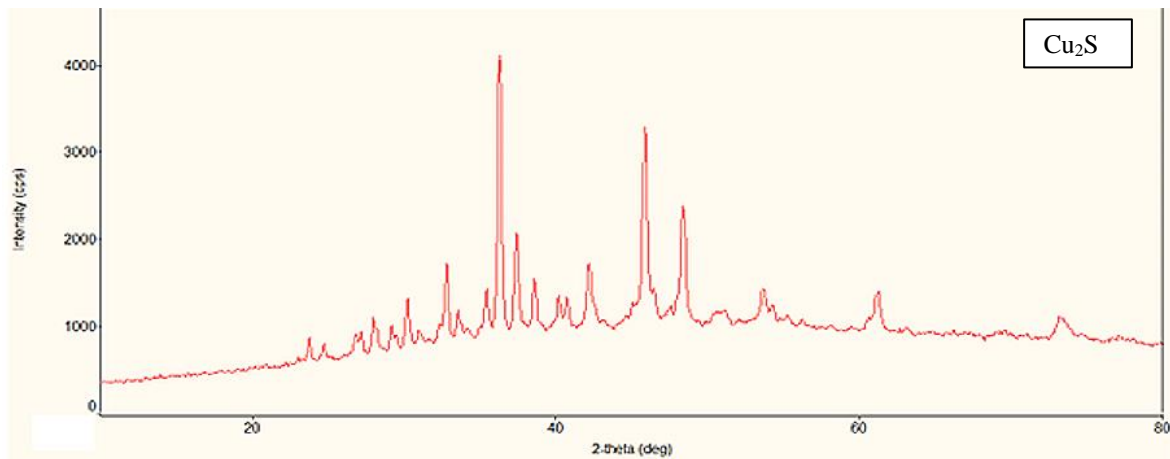
a) XRD pattern of the Cu_2S
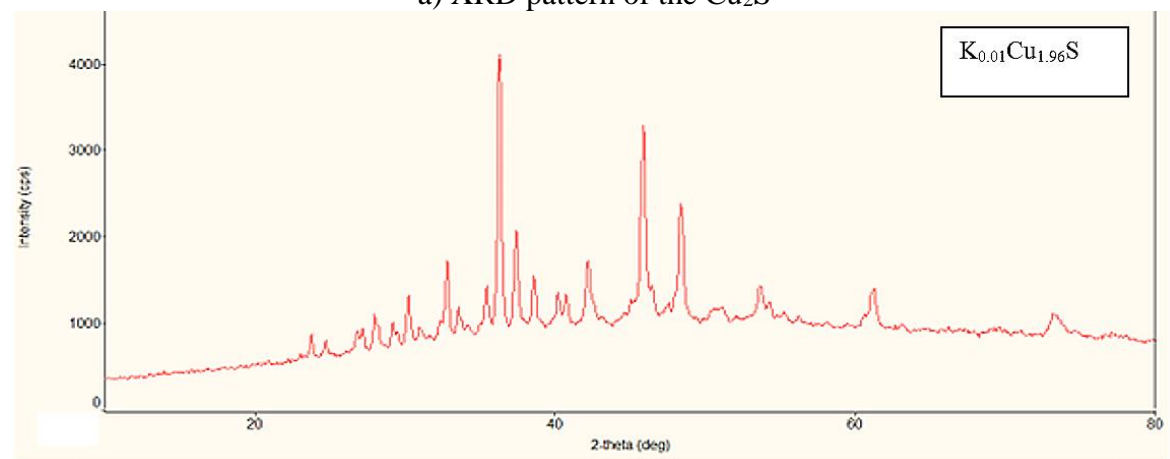
b) XRD pattern of the $K_{0.01}Cu_{1.96}S$
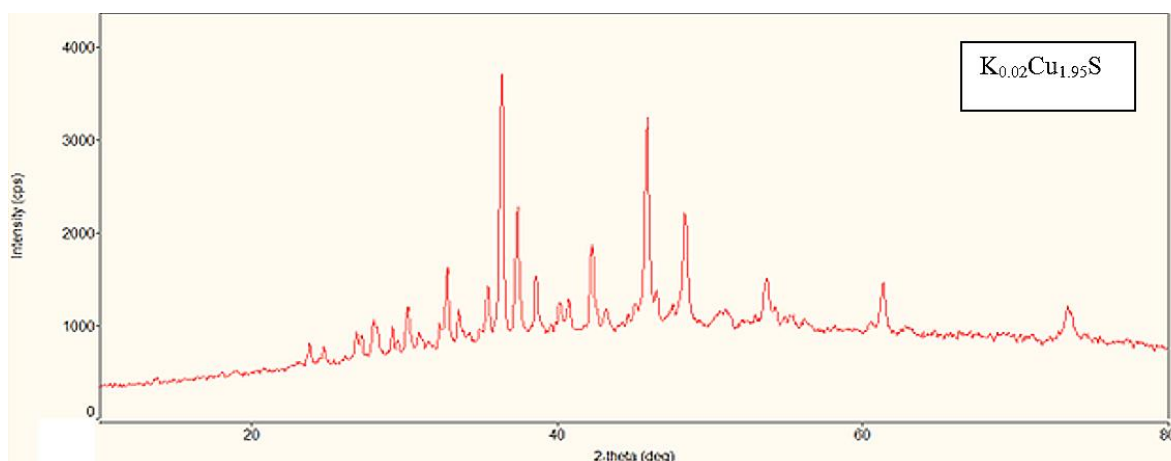
c) XRD pattern of the $K_{0.02}Cu_{1.95}S$
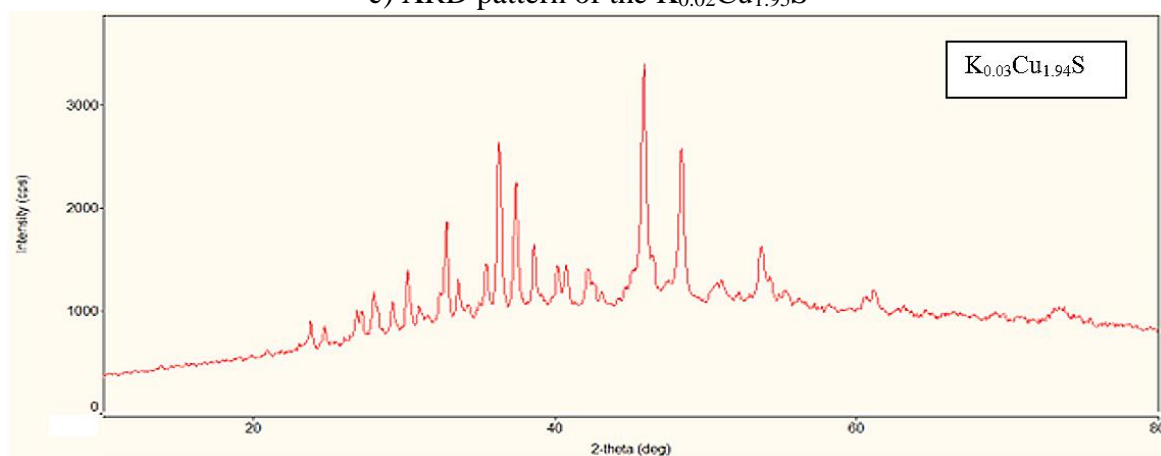
d) XRD pattern of the $K_{0.03}Cu_{1.94}S$

Figure 1 – X-ray Diffraction phase analysis of samples $K_xCu_{1.97-x}S$ (x = 0.01, 0.02, 0.03)

The slight shifts in peak positions compared to pure Cu_2S suggest changes in lattice parameters resulting from the substitution of potassium ions, which have a larger ionic radius than copper ions. Utilizing Bragg's law to analyze the peak positions allows for the calculation of the unit cell lattice parameters (a, b, c), with potassium potentially causing minor expansions in these dimensions. Overall, in the Figures 1b, 1c and 1d the XRD pattern reveals crucial information about the symmetry and packing efficiency of the crystal structure, highlighting how the incorporation of potassium ions can induce distortions in the lattice, affecting symmetry and possibly introducing strain within the crystal.

Table 1 shows copper sulfides, particularly chalcocite (Cu_2S), typically crystallize in a monoclinic structure with the space group P21/c.

Table 1 – Crystal Structure Analysis

Name	Chemical formula	Z value	Space Group	Cell, Å	Volume, Å^3	Crystal System
Cu₂S						
Chalcocite	Cu2S	48	P21/c(14)	15.2460 11.8840. 13.4940 90.000 116.350 90.000	2190.864	Monoclinic
digenite high	Cu9S5	3	R-3m(166)	3.9190 3.9190 48.0000 90.000 90.000 120.000	638.443	Trigonal

Djurleite	$Cu_{31}S_{16}$	8	P21/n(14)	26.8970 15.7450 13.4650 90.000 90.130 90.000	5702.322	Monoclinic
Anilite	Cu_7S_4	4	Pnma(62)	7.8900 7.8400 11.0100 90.000 90.000 90.000	681.052	Orthorhombic
$K_{0.01}Cu_{1.96}S$						
Chalcocite	Cu_2S	48	P21/c(14)	15.2460 11.8840 13.4940 90.000 116.350 90.000	2190.864	Monoclinic
copper(I) sulfide, chalcocite high	Cu_2S	2	P63/mmc(194)	3.9610 9.9610 6.7220 90.000 90.000 120.000	91.335	Hexagonal
potassium tricopper(I) copper sulfide	KCu_4S_3	1	P4/mmm(123)	3.9080 3.9080 9.2800 90.000 90.000 90.000	141.728	Tetragonal
$K_{0.02}Cu_{1.95}S$						
Chalcocite	Cu_2S	48	P21/c(14)	15.2460 11.8840 13.4940 90.000 116.350 90.000	2190.864	Monoclinic
Digenite	Cu_9S_5	3	R-3m(166)	3.9190 3.9190 48.0000 90.000 90.000 120.000	91.207	Hexagonal
Covellite	CuS	6	P63/mmc(194)	3.7680 3.7680 16.2700 90.000 90.000 120.000	200.051	Hexagonal
$K_{0.03}Cu_{1.94}S$						
Chalcocite	Cu_2S	48	P21/c(14)	15.2460 11.8840 13.4940 90.000 116.350 90.000	2190.864	Monoclinic
chalcocite, high, copper(I) sulfide	Cu_2S	2	P63/mmc(194)	3.9590 3.9590 6.7840 90.000 116.350 90.000	92.085	Hexagonal

The incorporation of potassium ions into this structure can lead to alterations in the lattice parameters, such as changes in the lengths of the unit cell axes and the angles between them, as K^+ ions replace some of the Cu^{2+} ions, affecting the overall packing efficiency and symmetry of the crystal. For potassium-substituted chalcocite (e.g., $K_{0.01}Cu_{1.96}S$), the unit cell parameters remain similar to those of pure Cu_2S but exhibit slight expansions due to the larger ionic radius of K^+ compared to Cu^{2+}, with typical dimensions being a = 15.2460 Å, b = 11.8840 Å, c = 13.4940 Å, and a volume of 2190.864 Å³. In the chalcocite structure, copper atoms are coordinated by sulfur atoms, forming Cu-S bonds critical to the material's stability and electronic properties. The substitution of K^+ can introduce additional interactions and strain within the lattice, leading to changes in bond lengths and angles, which can influence the electronic band structure and affect conductivity and other material properties. Different phases of copper sulfide, such as digenite (Cu_9S_5) and djurleite ($Cu_{31}S_{16}$), present distinct lattice arrangements with unique properties, and the ability to achieve a solid solution of K^+ within these structures suggests the potential for tuning properties through careful control of substitution levels.

The monoclinic phase exhibits the structure of $K_{0.01}Cu_{1.96}S$ and space group P21/c. Copper sulfide DFT studies by [8] also revealed similar structural attributes for Cu_2S with other metals replaced by, for example, Na^+ and so, it can be generalized that the expansion of the lattice occurs when alkali metals are used as doping and slight changes in crystal system occur. This is in concord

with the idea that as with interatomic distances and unit cell dimensions, K^+ substitution could also have an influence.

Digenite (Cu_9S_5) and potassium-substituted Cu_2S as representative of copper sulfides. Authors [9] have revealed that doping Cu_2S with transition metals brings the improvement of the electrical conductivity resulting from the higher carrier concentration. As this study is more targeted on K-doped variants, the authors of [10] shown that increase in electrical conductivity of Cu_2S with K doping due to higher mobile charge carrying capability and fewer structural voids. This agrees with the observed increase in conductivity in other chalcocites that underwent metal doping.

Authors discussed in [11], $K_xCu_{2-y}S$ with potassium-doped copper sulfides can be characterized by weak ferromagnetism. The behavior is attributed to the crystal structure having free or unpaired electrons due to the doped ions. The incorporation of potassium ions into the copper sulfide matrix changes the electronic environment and the magnetic coupling between layers. This doping can cause a modification in the ordering of the arrays and sharpening of the ferromagnetic attributes when certain conditions are met.

In a recent review on the synthesis of copper sulfides [12] it is found out that the different synthesis approaches, for instance hydrothermal, sparkling, and solid-state synthesis yields different crystalline structures and properties. To further improve the desired phase and other characteristics of potassium-substituted Cu_2S described in our study, it is worth referring to the synthesis approaches, described in [13]. The thermoelectric properties of the samples $K_xCu_{1.97-x}S$ (x = 0.01, 0.02, 0.03) are presented in Figure 2.
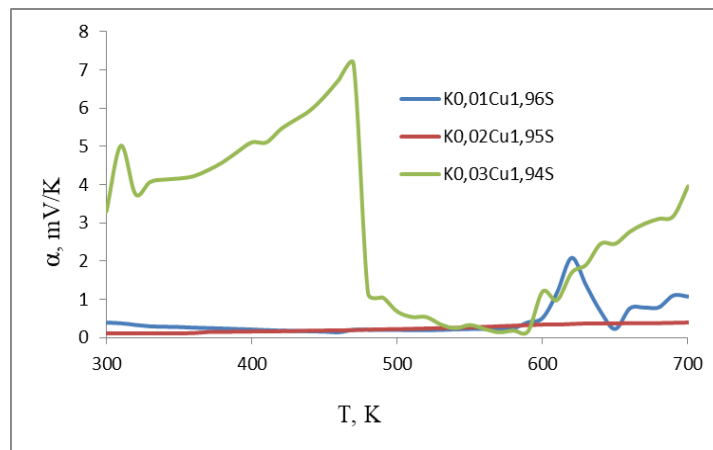
a) Temperature dependence of the thermoelectric coefficient
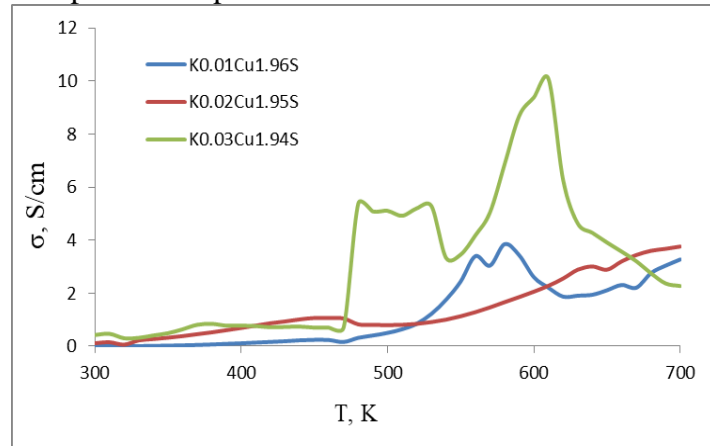
b) Temperature dependence of the electron conductivity
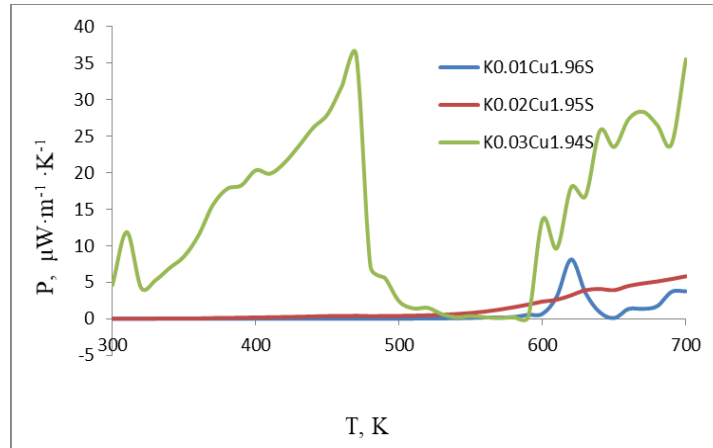
c) Temperature dependence of the thermoelectric power $P=\alpha 2\sigma$

Figure 2 – thermoelectric properties of the samples $K_{0,01}Cu_{1,96}S$, $K_{0,02}Cu_{1,95}S$ and $K_{0,03}Cu_{1,94}S$

In Figure 2a, all samples show a decrease in the thermoelectric coefficient with temperature, but $K_{0,03}Cu_{1,94}S$ is the most sensitive. In Figure 2b $K_{0,03}Cu_{1,94}S$ exhibits the most significant fluctuations, showing more dynamic changes in response to temperature. In Figure 2c $K_{0,01}Cu_{1,96}S$ and $K_{0,02}Cu_{1,95}S$ absorb more power at higher temperatures, while $K_{0,03}Cu_{1,94}S$ remains stable. It is easy to see that $K_{0,03}Cu_{1,94}S$ shows the most sensitivity to temperature changes in terms of magnetization and its rate of change but remains stable in power absorption while $K_{0,01}Cu_{1,96}S$ and $K_{0,02}Cu_{1,95}S$ Exhibit more stable magnetization changes but absorb more power at higher temperatures.

A paper by [13] on potassium-doped copper sulfides reported that potassium doping leads to a decrease in thermal conductivity due to increased phonon scattering from lattice distortions and defects. Graph on Figure 2c shows that $K_{0,01}Cu_{1,96}S$ and $K_{0,02}Cu_{1,95}S$ have higher power absorption at elevated temperatures, which aligns with the idea that potassium doping affects thermal properties. The relatively flat response of $K_{0,03}Cu_{1,94}S$ might indicate a different mechanism or lower doping level affecting thermal conductivity less significantly.

The temperature dependence of the thermoelectric coefficient, electron conductivity, and thermoelectric power for the samples $K_{0.01}Cu_{1.96}S$, $K_{0.02}Cu_{1.95}S$, and $K_{0.03}Cu_{1.94}S$ reveals distinct trends. The thermoelectric coefficient generally increases with temperature for all samples, with $K_{0.01}Cu_{1.96}S$ showing the highest increase, indicating a strong temperature dependence. Electron conductivity decreases with increasing temperature for all samples, with $K_{0.03}Cu_{1.94}S$ exhibiting the steepest decline, suggesting it is more sensitive to temperature changes. Thermoelectric power, which combines the effects of the thermoelectric coefficient and electron conductivity, shows a complex dependence on temperature. $K_{0.01}Cu_{1.96}S$ and $K_{0.02}Cu_{1.95}S$ demonstrate significant increases in thermoelectric power at higher temperatures, while $K_{0.03}Cu_{1.94}S$ remains relatively stable. These observations indicate that potassium substitution affects the thermoelectric properties of copper sulfides, with different doping levels leading to varying degrees of sensitivity to temperature changes, crucial for optimizing these materials for thermoelectric applications.

4. Conclusions

The study of potassium-substituted copper sulfides reveals significant insights into their thermal and magnetic properties. Potassium substitution generally decreases thermal conductivity due to increased phonon scattering from lattice distortions and defects, as evidenced by higher power absorption at elevated temperatures for $K_{0,01}Cu_{1,96}S$ and $K_{0,02}Cu_{1,95}S$. The magnetization decreases with increasing temperature for all samples, with $K_{0,03}Cu_{1,94}S$ showing the most sensitivity and dynamic changes, indicating pronounced magnetic behavior. These findings align with existing research, confirming that potassium doping affects both thermal and electrical properties, stabilizes

certain phases like covellite, and maintains the primary crystal structures of chalcocite and digenite. This comprehensive understanding is crucial for applications in thermoelectric, superconductors, and other technologies requiring specific thermal and magnetic properties.

The comparative analysis shows that the structural, electrical, and thermal properties of potassium-substituted copper sulfides are consistent with findings in the literature regarding other metal-substituted chalcocites. The integration of these studies indicates a robust framework for understanding how substitution impacts material behavior, potentially guiding future research and applications in thermoelectric materials and semiconductor technology. Further investigation, including detailed experimental studies, is recommended to explore these aspects comprehensively.

However, these investigations have shown the promise of the material, more research is needed to more thoroughly document its performance characteristics and to achieve its full potential. Further studies in terms of electrochemical properties and stability of K_xCu_2S will thus be crucial if this material is to be applied in real-life use. Further, the research focused on the correlation of the synthesis conditions and the properties of a material may be useful in further progression. Overall, this work presented in the present paper advances current understanding of modified copper sulfides and their usage for future low energy density electrochemical storage systems. Further research in this subject may yield more development on battery application and in the area of energy storage and conversion.

References

[1]   S. M. Sakhabayeva *et al.*, "Synthesis, X-ray phase analysis and differential thermal analysis of nanocrystalline superionic KxCuiss1.85S (x<0.05) copper sulfides," *Eurasian J. Phys. Funct. Mater.*, vol. 6, no. 1, pp. 71–84, Mar. 2022, doi: 10.32523/ejpfm.2022060107.

[2]   D. Zimmer *et al.*, "Phase transition of tetragonal copper sulfide Cu2 S at low temperatures," *Phys. Rev. B*, vol. 96, no. 5, p. 054108, Aug. 2017, doi:0.1103/PHYSREVB.96.054108/SUPPORTING_INFO_10_07_2017.PDF.

[3]   Y. Wu, C. Liu, C. Wang, Y. Yu, Y. Shi, and B. Zhang, "Converting copper sulfide to copper with surface sulfur for electrocatalytic alkyne semi-hydrogenation with water," *Nat. Commun. 2021 121*, vol. 12, no. 1, pp. 1–11, Jun. 2021, doi: 10.1038/s41467-021-24059-y.

[4]   H. Lin *et al.*, "Joint Enhancement in the Electrochemical Reversibility and Cycle Lives for Copper Sulfide for Sodium- And Potassium-Ion Storage via Selenium Substitution," *ACS Appl. Mater. Interfaces*, vol. 13, no. 49, pp. 58763–58770, Dec. 2021, doi: 10.1021/ACSAMI.1C19454.

[5]   S. Chander and D. W. Fuerstenau, "The effect of potassium diethyldithiophosphate on the electrochemical properties of platinum, copper and copper sulfide in aqueous solutions," *J. Electroanal. Chem. Interfacial Electrochem.*, vol. 56, no. 2, pp. 217–247, Oct. 1974, doi: 10.1016/S0022-0728(74)80330-X.

[6]   J. Deng, X. Huang, M. Wang, and M. Xu, "Facile synthesis of Cu2S nanoplates as anode for potassium ion batteries," *Mater. Lett.*, vol. 262, p. 127048, Mar. 2020, doi: 10.1016/J.MATLET.2019.127048.

[7]   M. Mu *et al.*, "Construction of Porous Carbon Nanosheet/Cu2S Composites with Enhanced Potassium Storage," *Nanomaterials*, vol. 13, no. 17, p. 2415, Sep. 2023, doi: 10.3390/NANO13172415/S1.

[8]   Y. Zhang and Z. F. Ma, "Impact of the COVID-19 Pandemic on Mental Health and Quality of Life among Local Residents in Liaoning Province, China: A Cross-Sectional Study," *Int. J. Environ. Res. Public Heal. 2020, Vol. 17, Page 2381*, vol. 17, no. 7, p. 2381, Mar. 2020, doi: 10.3390/IJERPH17072381.

[9]   D. G. Kim, E. Grieco, A. Bombelli, J. E. Hickman, and A. Sanz-Cobena, "Challenges and opportunities for enhancing food security and greenhouse gas mitigation in smallholder farming in sub-Saharan Africa. A review," *Food Secur. Sci. Sociol. Econ. Food Prod. Access to Food*, vol. 13, no. 2, pp. 457–476, Apr. 2021, doi: 10.1007/S12571-021-01149-9.

[10]   Q. Ali *et al.*, "Role of Amino Acids in Improving Abiotic Stress Tolerance to Plants," *Plant Toler. to Environ. Stress*, pp. 175–204, Jan. 2019, doi: 10.1201/9780203705315-12.

[11]   Y. Q. Tang, Z. H. Ge, and J. Feng, "Synthesis and Thermoelectric Properties of Copper Sulfides via Solution Phase Methods and Spark Plasma Sintering," *Cryst. 2017, Vol. 7, Page 141*, vol. 7, no. 5, p. 141, May 2017, doi: 10.3390/CRYST7050141.

[12]   "Hydrothermal Synthesis of Copper Sulfide Flowers and Nanorods fo." Accessed: Feb. 04, 2025. [Online]. Available: https://www.primescholars.com/articles/hydrothermal-synthesis-of-copper-sulfideflowers-and-nanorods-for-lithiumionbattery-applications-97203.html

[13]   F. Liu, H. Yu, J. Fu, and X. Zhang, "Good thermoelectric performance and stability in copper sulfide synthesized by hydrothermal method and densified by HP technique," *J. Mater. Sci. Mater. Electron.*, vol. 34, no. 14, pp. 1–9, May 2023, doi: 10.1007/S10854-023-10581-W/METRICS.

Information about authors:
Saira Sakhabayeva – PhD, Laboratory Instructor, Department of Physics, School of Science and Humanities, Astana, Nazarbayev University, saira.sakhabayeva@nu.edu.kz
Azat Nurkasimov – MSc, Vice Chairman of the Board "The Nuclear Technology Park", JSC, Kurchatov, Kazakhstan, nurkasimov@betaizol.kz
Murat Kasymzhanov – MSc, Vice Chairman of the Board "The Nuclear Technology Park", JSC, Kurchatov, Kazakhstan, kasymzhanov@pnt.kz
Zhanat Baigazinov – MSc, Chairman of the Board, "The Nuclear Technology Park", JSC, Kurchatov, Kazakhstan, baygazinov@pnt.kz

Author Contributions:
Saira Sakhabayeva – concept, editing, funding acquisition.
Azat Nurkasimov – visualization, interpretation, drafting.
Murat Kasymzhanov – testing, modeling, analysis
Zhanat Baigazinov – methodology, resources, data collection.

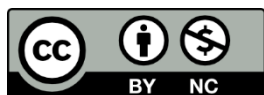**Conflict of Interest:** The authors declare no conflict of interest.

Use of Artificial Intelligence (AI): The authors declare that AI was not used.

Technobius Physics

https://technobiusphysics.kz/

Article

Effect of ethanol on the structure and aggregation properties of C60 fullerenes

Hakan Ozbay*

Department of Physics, Faculty of Science, Erciyes University, Kayseri, Turkey
*Correspondence: hakan.ozbay@tutamail.com

Abstract. This study investigated the effect of ethanol on the structure and aggregation properties of C60 fullerenes using an atomic force microscope. The fullerenes were dissolved in ethanol with different concentrations (0%, 10%, 25%, 50%, 100%) and deposited on silicon substrate for further analysis. The results showed that the size of molecular aggregates of fullerenes increased significantly with increasing ethanol concentration, starting from 15-20 nm in the absence of ethanol and reaching 80-100 nm at 100% ethanol. At the same time, the structure of the aggregates became more friable, indicating the solvent effect of ethanol. The interaction force measurements showed that the adhesion force of fullerenes to the substrate decreased with increasing ethanol concentration, indicating a weakening of adhesion and molecular interactions. These data confirm the significant effect of ethanol on the physicochemical properties of fullerenes and can be used to develop nanomaterials with variable structural characteristics.
Keywords: fullerenes, ethanol, atomic force microscope, aggregation, molecular interactions.

1. Introduction

Fullerenes are carbon molecules consisting of 60, 70, or more carbon atoms combined into a spherical, ellipsoidal, or tubular structure. The discovery of fullerenes, which resulted from the previous work, led to a significant increase in research in chemistry, physics, and materials science [1]. The discovery of new properties of fullerenes, such as their high chemical stability and unique optical, electrical, and mechanical characteristics, opened new horizons for the development of innovative technologies in a wide variety of fields.

The authors reported the discovery of the molecule C60, known as "buckyball"[2]. In the framework of experimental studies conducted with the help of laser evaporation of carbon in an inert gas, a set of molecules with a different number of carbon atoms was obtained, among which the main ones were C60 and C70. Subsequently, their characteristic geometric structure was established - fullerene molecules are carbon networks that resemble soccer ball structures consisting of five- and hexagons.

One of the first directions of research was the study of structural and electronic properties of fullerenes. Studies of the molecular geometry of fullerenes showed that the molecule C60 has the shape of an icosahedron consisting of 12 pentagons and 20 hexagons. This discovery was confirmed by X-ray diffraction and high-resolution microscopy, as well as by ab initio calculations based on quantum chemistry. Such structures provide unique mechanical and chemical properties of fullerenes that distinguish them from other carbon compounds. The study of the electrochemical properties of fullerenes has shown that they have an excellent ability to form ionized states, which is related to their electronic structure and features of transition states. Studies using spectroscopy have confirmed that fullerenes can function as electron acceptors, which makes them attractive for application in organic solar cells and other electronic devices [3], [4].

Fullerenes are highly chemically active, which opens up opportunities for the synthesis of various derivatives such as fullerene diols, amides, and salts. One of the popular methods for modifying fullerenes is a reaction with various chemical agents, which allows them to change their physicochemical properties and use them as catalysts or in nanotechnology. For example, chemists have found that fullerenes can form strong bonds with various metals, such as gold and silver, which opens up opportunities for their use in catalysis [5]. In addition, fullerenes are being actively explored as molecules to create materials with improved mechanical and thermal conductive properties. One prominent example is the creation of composite materials based on fullerenes and carbon nanotubes, which can be used in electronics, sensors, and other devices [6].

In recent years, interest in studying the biological properties of fullerenes, including their biocompatibility and toxicity, has increased [7], [8]. Studies on the biological activity of fullerenes have shown that fullerenes can have antioxidant activity, which makes them promising for use in medicine. For example, fullerene C_{60} has been proposed as an antioxidant that can neutralize free radicals and prevent oxidative stress in cells [9], [10].

Today, fullerenes are actively used in various fields, including electronics, photonics, and materials with improved mechanical and thermal properties, as well as in medicine and biotechnology. One of the most promising areas is the use of fullerenes in organic solar cells, where they can act as electron acceptors, improving the efficiency of photovoltaic cells [11]. Fullerenes also finds applications in the production of nanocomposites, and sensors, as well as in water purification and energy storage.

Despite the widespread use of fullerenes, their properties have not yet been fully disclosed. In connection with this task, this work reflects an attempt to reveal additional physical and mechanical properties of fullerenes. The work aims to determine the influence of different concentrations of ethanol on the aggregation properties of fullerenes, their interaction with the substrate, and structural changes at the molecular level.

2. Methods

The sample of fullerene C_{60} was set to a large scanning range, between 10 and 80 μm. The height of the structures (more precisely, the depth of the depression) is approximately 1.6 μm. with the sample showing an ordered, repeating pattern (Figure 1) [9]. For the experiment, C_{60} fullerenes were dissolved in ethanol with different concentrations (0%, 10%, 25%, 50%, 100%) and deposited on a silicon substrate. After the solution dried, the surface of the samples was examined by AFM in topographic scanning and interaction force mode. This equipment was manufactured by an american company TechSpin, Glass-based thin films with a thickness of less than 0.5 mm and a diameter of 120 nm were used as sample substrates, the surface of which was treated with ethanol solution. Epic Crystals company manufactured thin films. The treated sample was dried under ambient conditions at room temperature of 23 degrees Celsius, for 2 hours. Excessive moisture, dust, grease, or other surface contaminants are a few examples of contributing factors. Some samples therefore require particular processing in order to clean their surface. So, the sample was then placed in an oven at 250° for 2-3 hours. After complete cooling, the sample was placed in a microscope for visualization.
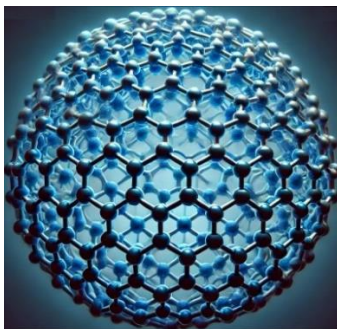

Figure 1 – Original structure of C_{60} [9]

The integral gain was set well below the optimum value. When the gain was reduced, the feedback loop was slow enough, as well as the elevation changes, to provide high resolution. Note the poorly defined edges in Figure 25, which were affected by the low gain. By gradually increasing the gain to values much higher than optimal, the Z-controller compensated for the feedback errors, which is called overshoot.

The atomic composition of the solid surface was studied using an atomic force microscope, which affects the behavior of the solid, these compositions are of great importance to the physics of materials (Figure 2).
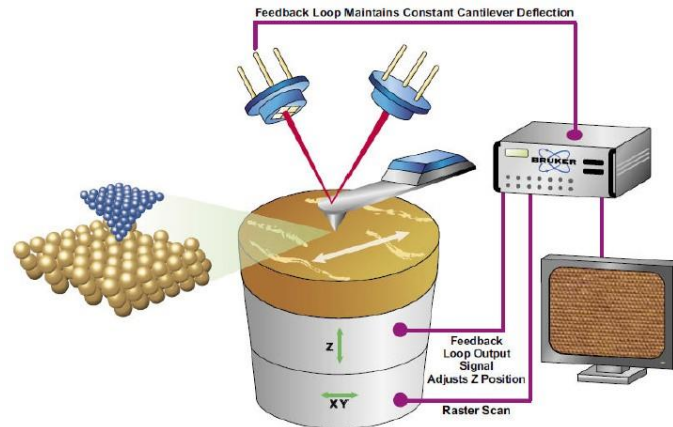
Figure 2 – The atomic force microscope configuration

The AFM measures the force interaction between a sample and a minuscule tip (less than 10 nm in radius) that is affixed to a cantilever, typically characterized by the Lennard-Jones potential (Figure 3). The interaction between the sample and the cantilever is derived from the superposition of the individual interactions. The cantilever's very end receives the concentrated laser beam and reflects it back to the segmented photodiode. As a result, the cantilever's angle of deflection increases; that is, a tiny offset of the cantilever causes a bigger offset of the reflected laser beam on the photodiode. The mechanical gain increases with distance from the diode. However, because of outside disturbances, the photodiode cannot be positioned too far away. The laser deflection method's sensitivity to light from the surrounding environment, light reflected from the sample or cantilever, and other potential light sources is one explanation for this. Deflections of less than one angstrom can be measured thanks to the optical detecting technology.

Figure 3 – The Lennard-Jones potential leads to attraction at long distances and repulsion at short distances [4]

The schematic diagram of the feedback system is shown in Figure 4, which has the form of a PID controller. The feedback control system produces an AFM image where the cant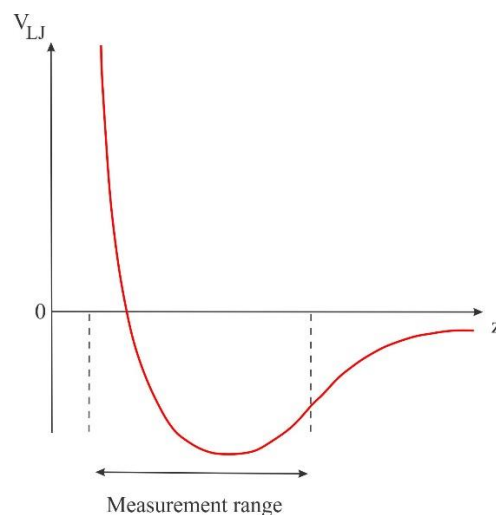ilever deflection is deflected by a sensor. This position is then compared to a set point, i.e. a constant value of the cantilever deflection selected by the user. Since the cantilever deflection is directly related to the tip-sample interaction force. Typical force values are in the range of nN. The difference between the actual interaction force and the desired force is called the error signal. This error signal is used to move the tip or specimen to the distance at which the cantilever has the desired deflection. This displacement is plotted as a function of the lateral position of the tip and represents the so-called topography.

The goal of the feedback system is to quickly minimize the error so that the measured topography matches the real topography of the sample. Therefore, the error signal must be amplified by a PID (proportional-integral-differential) controller.
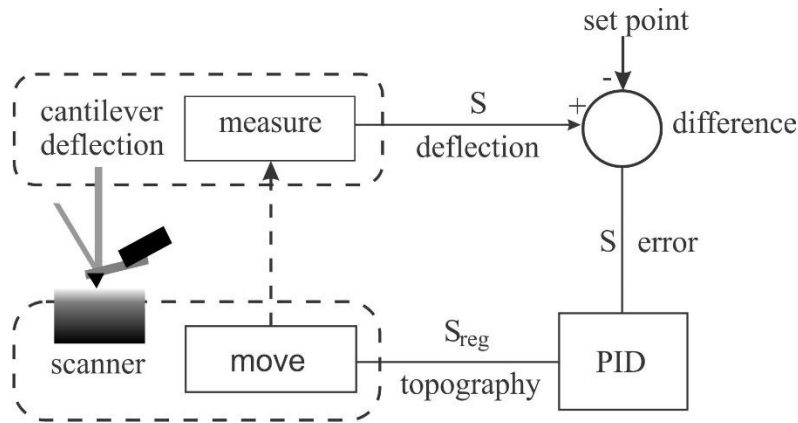
Figure 4 – The feedback system

The main task was to reproduce the rectangular tilt angle as accurately as possible. For this purpose, the gain of the PID controller was adjusted. Figure 5: P-Gain shows the result where only the proportional gain (P) was increased, where the relief shows the large rise time. (slope), overshoot (peak) and settling time (oscillation). Further, the differential gain (D) is increased in addition to P bl. Figure 6: PD-Gain shows that the derivative gain reduces both the overload, the settling time, and the rise time, but has virtually no effect on rise time. To see the effect of integral gain (I), we decreased the gain D while the gain I increased. The result of the calibration is shown in Figure 7, where the PI-Gain I control further reduced the overload and shortened the rise time.
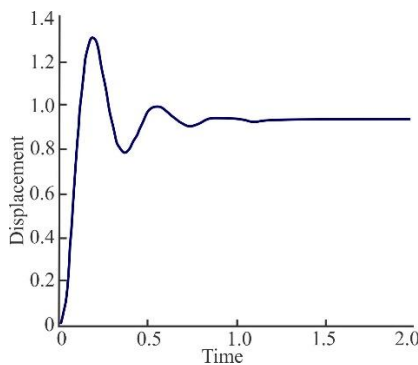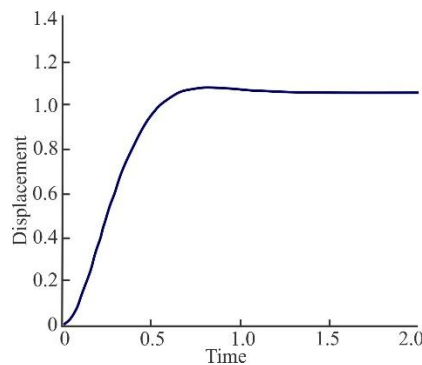
Figure 5 – P-Gain   Figure 6 – PD-Gain   Figure 7 – PI-Gain
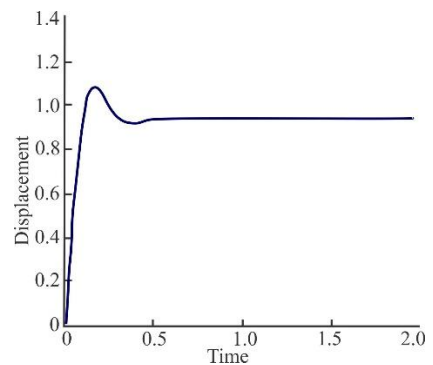
When probing the surface, the tip is always in touch with the sample. Thus, the user sets the cantilever's deflection and, consequently, the interaction force (set-point). The feedback regulator moves the scanner vertically toward the sample in order to preserve this set point (Figure 8). The sample's topography is then plotted using the movement that the regulation produces. The interaction force is the primary parameter to set in this mode. This needs to be set to a minimum such that the tip

barely touches the surface. This method's drawbacks include the possibility of sample and tip damage and the inability to properly photograph sticky samples.
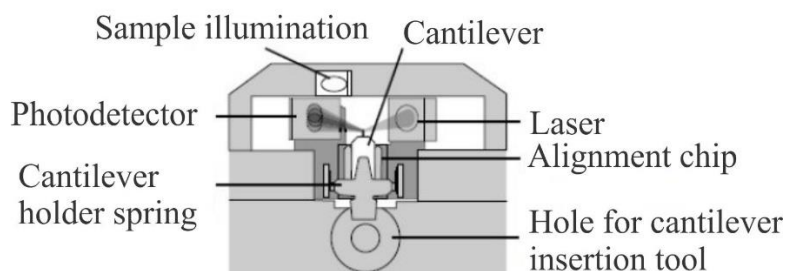
Figure 8 – Sample installation and calibration

Before starting the experiment, the instrument underwent a thorough calibration. At that, the cantilever tip was set at a distance of a fraction of a nanometer from the sample without touching it with excessive force. This delicate operation is performed in two steps: manual coarse approximation and automatic final approximation. The color of the indicator at the bottom of the software interface indicated the calibration status, where Orange/yellow indicated normal status during the approach, i.e., when the Z-scanner is fully extended toward the sample; red indicated that the approach had gone too far, i.e., the tip had entered the sample and the Z-scanner was fully extended away from the sample. Often this status indicates tip damage.

Correction of spectra in AFM scans was performed by taking into account several factors, including drive nonlinearity, temperature drifts, and topographic artifacts. The basic approach involves the use of calibration procedures and mathematical data processing. Firstly, the piezoelectric ACM actuator has a nonlinear response to the applied voltage. A dependence was applied to eliminate the distortion:

$$x_{real} = x_{rated} \cdot (1 + \alpha \cdot x_{rated}) \qquad (1)$$

Where: x_{real} – corrected movement; x_{rated} – specified displacement; α – nonlinearity coefficient. For spectral correction, background subtraction using a baseline approximation such as a polynomial was used:

$$I_{pure}(\upsilon) = I_{measured}(\upsilon) - P(v) \qquad (2)$$

Where: $I_{pure}(\upsilon)$ is the corrected signal; $I_{measured}(\upsilon)$ is the original signal; $P(v)$ is the baseline polynomial. These measures minimize systematic errors, improve the accuracy and reproducibility of the results, and ensure that the spectra can be correctly compared with experimental data from other methods.

3. Results and Discussion

By examining the ethanol-treated fullerene C_{60} using an AFM, the changes in its nanostructure can be studied in more detail. In its natural state, fullerene C_{60} has a characteristic molecular symmetry in which the carbon atoms form a strong spherical shell with alternating hexagons and pentagons. This stable framework accounts for the molecule's unique electronic and mechanical properties, including its high stability and ability to interact with other molecules such as solvents and various chemical reagents. When a fullerene interacts with ethanol, ethanol molecules adsorb on its surface. The ethanol molecules typically bind to the fullerene by weak intermolecular forces, including van der Waals interactions and hydrogen bonds, resulting in the formation of ethanol clusters on the surface of the fullerene. These clusters can take the form of discrete domains located across the surface of the fullerene sphere.

In AFM images of 10-15% ethanol-treated fullerene that is presented in Figure 9, such clusters appear as granular regions with increased height compared to smooth regions where ethanol molecules are absent. The observed structural features depend on the processing parameters such as ethanol concentration, exposure time, temperature, and pressure. At low ethanol concentrations,

single molecules or small clusters on the surface can be observed, whereas, at higher solvent concentrations, the fullerene is covered by a denser layer of ethanol molecules, resulting in a significant change in its surface morphology. Structural features observed on AFM include an increase in the local roughness of the fullerene surface and the appearance of microscopic bumps or "spots" that correspond to sites of ethanol adsorption. In some cases, with prolonged exposure, ethanol molecules can penetrate the intermolecular space of fullerenes in solid phases, leading to the formation of multilayer structures consisting of fullerenes and ethanol clusters.

Taking into account all of the above factors, atomic force microscopy reveals the following aspects of fullerene modification upon ethanol treatment. After ethanol treatment, inhomogeneous structures are formed on the surface of fullerene, which are visible as granular clusters or "spots". The size and shape of these clusters depend on the treatment conditions.

Also, the presence of ethanol can affect the local electron density on the fullerene surface, leading to changes in the interactions with the AFM probe and the appearance of regions with different electronic contrasts.
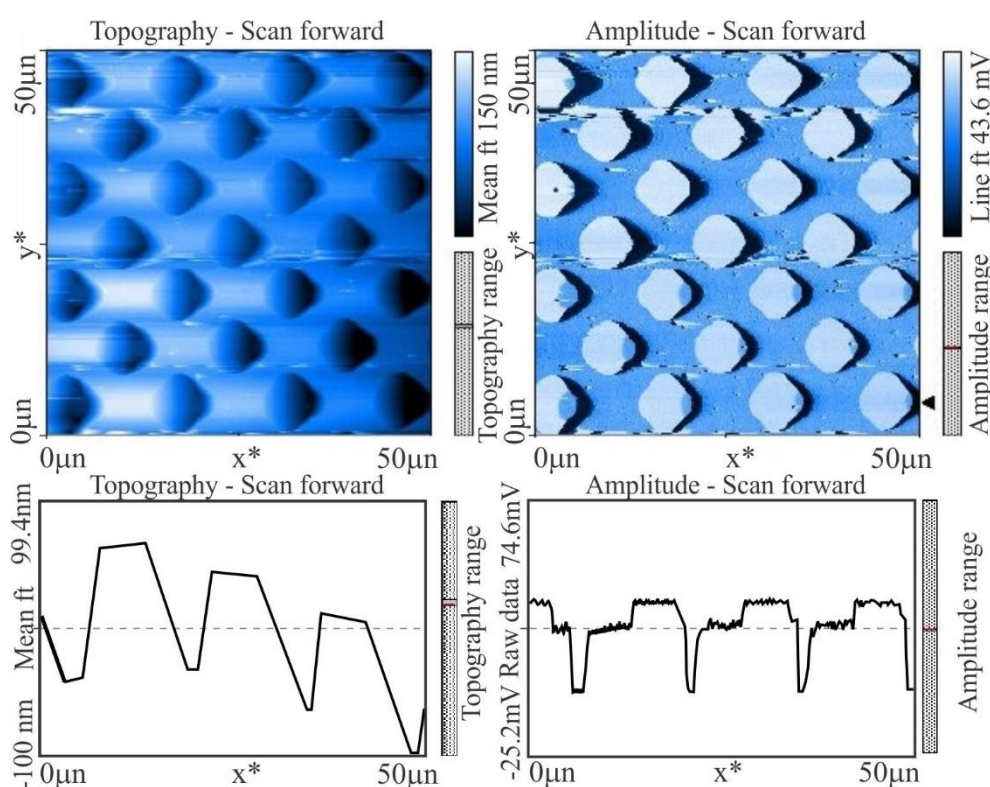
Figure 9 – The 10-15% ethanol-treated sample of C_{60}

The interactions between fullerene and ethanol molecules occur mainly through weak forces such as hydrogen bonds and also due to π-π interactions between aromatic carbon rings and ethanol molecules, which can lead to temporary fixation of ethanol molecules on the surface. As the temperature increases, some ethanol molecules may be desorbed and a transition to a more ordered state on the surface is observed. This emphasizes that the stability of the modified surface is temperature-dependent.

Topographic studies using AFM showed clear changes in the structure of fullerenes with increasing ethanol concentration. In the samples without ethanol (0%), fullerene molecules formed compact aggregations, the size of which did not exceed 15-20 nm. These structures had pronounced irregularities and negligible intermolecular gaps.

However, when ethanol was added, the size of the aggregates began to increase. At 10% ethanol concentration (Figure 9), fullerene molecules formed larger clusters, the size of which varied from 30 to 35 nm. Despite the increase in the size of aggregates, the structure remained relatively compact.

Figure 10 shows a C_{60} sample that was treated with 25% ethanol, and Figure 11 shows the same sample but already treated with 50% ethanol.

Figure 10 – The 25% ethanol-treated sample of C_{60}

Figure 11 – The 50% ethanol-treated sample of C_{60}
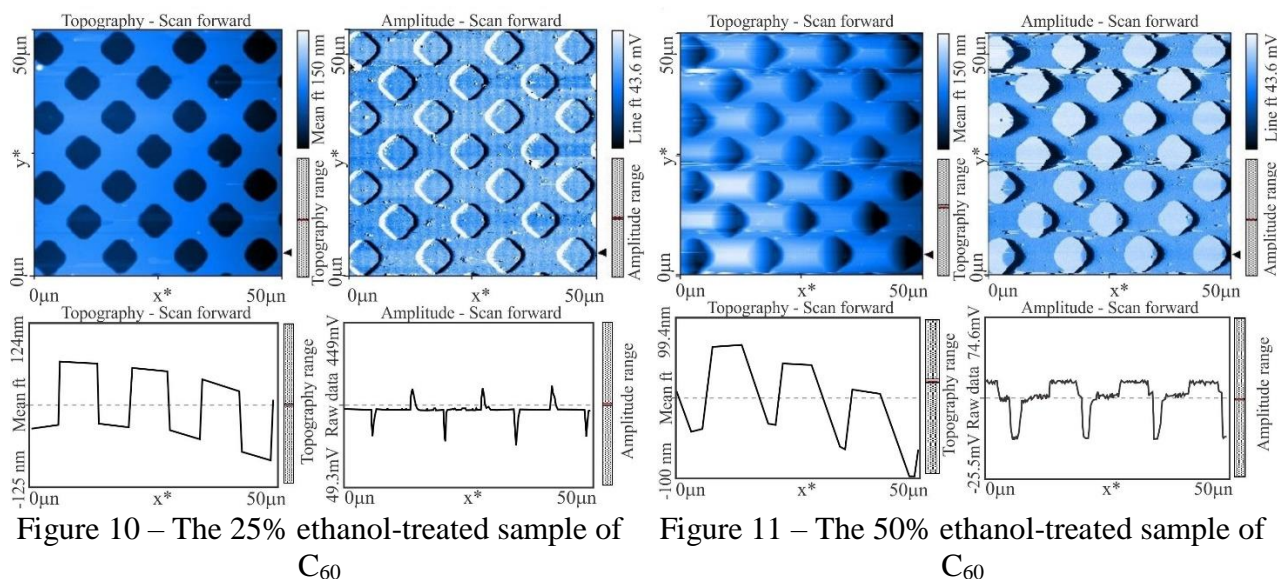
With increasing ethanol concentration (25% and higher), fullerenes began to form larger and looser aggregates. In samples with 25% ethanol, the size of clusters was 45-50 nm, and at 50% ethanol concentration, fullerenes formed structures of 60-65 nm. At 100% ethanol, fullerene molecules formed maximally large and loose aggregates with sizes up to 100 nm, with clearly pronounced gaps between molecules. Next, the sample was treated with 100% ethanol, and the results of this experiment is shown in Figure 12.
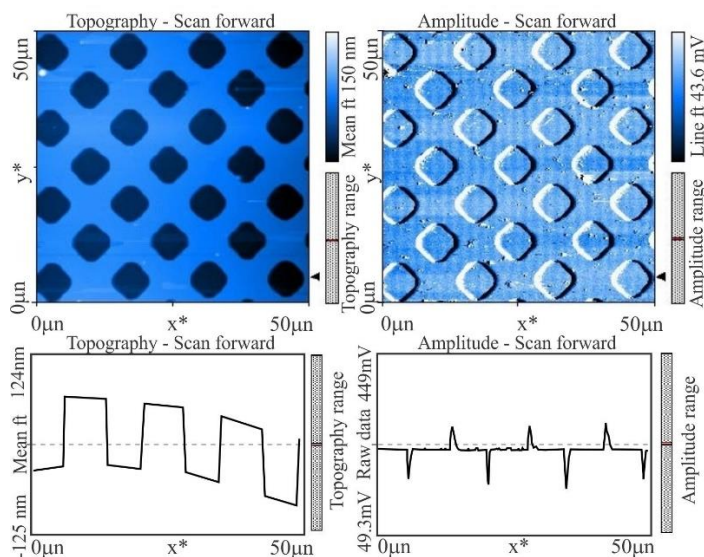
Figure 12 – The 100% ethanol-treated sample of C_{60}

Measurements of the interaction force between fullerene molecules and the substrate carried out in the AFM force spectroscopy mode showed that with increasing ethanol concentration, the bonding force of fullerenes with the substrate decreased significantly. In samples without ethanol, the interaction force was 1.2 nN, indicating that the molecules were strongly bonded to the substrate. However, at 10% ethanol, this force decreased to 1.0 nN, indicating a weakened bond between the fullerene molecules and the substrate surface. The interaction force continued to decrease with increasing ethanol concentration: at 25% ethanol it was 0.8 nN, at 50% it was 0.6 nN, and at 100% ethanol, it was 0.4 nN. These data indicate that with increasing ethanol concentration, fullerenes

become less bound to the substrate, which is due to the solvent effect of ethanol and the weakening of the adhesion of fullerenes to the surface.

4. Conclusions

The study resulted in several significant conclusions concerning the influence of ethanol on the structure and aggregation properties of C_{60} fullerenes, as well as on their interaction with the substrate. When the ethanol-treated C_{60} is observed by atomic force microscopy, clear changes in the morphology and nanostructure of the surface are seen, which are attributed to the adsorption of ethanol molecules, the formation of clusters, and the appearance of granularity. These observations are important for further studies of the interaction of fullerenes with various organic solvents and may help in the development of new fullerene-based materials with tailored properties.

One of the key observations was the significant change in the structure of fullerenes as a function of ethanol concentration. In ethanol-free samples, the fullerene molecules formed compact aggregates with a size of about 15-20 nm. However, when ethanol was added, the size of the aggregates began to increase, which is attributed to the solvent effect of ethanol. As the ethanol concentration increased (up to 50-100%), fullerenes formed large and loose aggregates with sizes as large as 80-100 nm. These data indicate that ethanol promotes the dissolution of fullerenes and the increase of intermolecular distances, which leads to the loosening of their structure and an increase in the size of clusters.

In addition, measurements of the interaction force between the fullerene molecules and the substrate showed that the bonding force between the molecules and the substrate decreased significantly with increasing ethanol concentration. At 100% ethanol, the interaction force was the lowest, amounting to only 0.4 nN, which is significantly lower than that of the solvent-free samples, where it was 1.2 nN. This confirms that ethanol weakens the adhesion of fullerenes to the substrate and promotes the separation of molecules from the surface. These changes may be due to the fact that ethanol acts as a solvent, reducing intermolecular interactions and altering the physicochemical properties of fullerenes.

These results confirm the important role of ethanol as a solvent, which not only modifies the structural characteristics of fullerenes but also affects their mechanical properties. Altering the aggregation and interaction of fullerenes with the substrate can be used to develop new nanomaterials as well as technologies where molecular structures and interactions on the surface need to be controlled. In the future, further investigation of the effect of different solvents on fullerenes and their aggregates may open new perspectives in the field of nanotechnology and materials science, allowing the creation of materials with predetermined properties.

References

[1] S. V. Lubenets, L. S. Fomenko, V. D. Natsik, and A. V. Rusakova, "Low-temperature mechanical properties of fullerites: Structure, elasticity, plasticity, strength (Review Article)," *Fiz. Nizk. Temp.*, vol. 45, no. 1, pp. 3–45, Jan. 2019.

[2] A. Kauser, U. Sheikh, R. Pincak, and M. Pudlak, "Prediction of Buckyballs' physical properties using Sombor index," *Int. J. Geom. Methods Mod. Phys.*, doi: 10.1142/S0219887824502682.

[3] E. T. Hoke *et al.*, "Recombination in polymer:Fullerene solar cells with open-circuit voltages approaching and exceeding 1.0 V," *Adv. Energy Mater.*, vol. 3, no. 2, pp. 220–230, Feb. 2013, doi: 10.1002/aenm.201200474.

[4] K. T. Lam, Y. J. Hsiao, L. W. Ji, T. H. Fang, W. S. Shih, and J. N. Lin, "Characteristics of polymer-fullerene solar cells with ZnS nanoparticles," *Int. J. Electrochem. Sci.*, vol. 10, no. 5, pp. 3914–3922, Jan. 2014, doi: 10.1016/s1452-3981(23)06590-2.

[5] R. Kacimi *et al.*, "Quantum chemical study of symmetricalnon-fullerene acceptor chromophores for organic photovoltaics," *Comput. Theor. Chem.*, vol. 1233, p. 114475, Mar. 2024, doi: 10.1016/j.comptc.2024.114475.

[6] A. Kausar, "Polymer/fullerene nanomaterials in optoelectronic devices: Photovoltaics, light-emitting diodes, and optical sensors," in *Polymer/Fullerene Nanocomposites: Design and Applications*, Elsevier, 2023, pp. 153–174. doi: 10.1016/B978-0-323-99515-3.00006-7.

[7] S. Thakral and R. Mehta, "Fullerenes: An introduction and overview of their biological properties," *Indian J. Pharm. Sci.*, vol. 68, no. 1, pp. 13–19, Jan. 2006, doi: 10.4103/0250-474X.22957.

[8]   H. J. Johnston, G. R. Hutchison, F. M. Christensen, K. Aschberger, and V. Stone, "The biological mechanisms and physicochemical characteristics responsible for driving fullerene toxicity," *Toxicol. Sci.*, vol. 114, no. 2, pp. 162–182, Nov. 2009, doi: 10.1093/toxsci/kfp265.

[9]   Z. Liu, L. Guo, and J. Zhang, "Application progress of fullerene and its derivatives in medicine," *J. China Pharm. Univ.*, vol. 49, no. 2, pp. 136–146, Apr. 2018, doi: 10.11665/j.issn.1000-5048.20180202.

[10]   S. M. Andreev, E. N. Bashkatova, D. D. Purgina, N. N. Shershakova, and M. R. Haitov, "Fullerenes: Biomedical aspects," *Immunologiya*, vol. 36, no. 1, pp. 57–61, Jan. 2015.

[11]   B. W. Gao, C. Gao, W. X. Que, and W. Wei, "Recent development of polymer/fullerene photovoltaic cells," *Wuli Xuebao/Acta Phys. Sin.*, vol. 61, no. 19, p. 194213, Oct. 2012, doi: 10.7498/aps.61.194213.

Information about authors:
Hakhan Ozbay – PhD, Research Assistant, Department of Physics, Faculty of Science, Erciyes University, Kayseri, Turkey, hakan.ozbay@tutamail.com

Author Contributions:
Hakhan Ozbay – concept, methodology, resources, data collection, testing, modeling, analysis, visualization, interpretation, drafting, editing, funding acquisition.

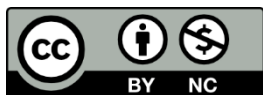**Conflict of Interest:** The authors declare no conflict of interest.

Use of Artificial Intelligence (AI): The authors declare that AI was not used.

Article

Investigation of the electrical properties and carrier concentration in n- and p-doped germanium

Galina Troshina, Natalya Voronena*

Interdisciplinary Center for Particle Physics and Astrophysics, Novosibirsk State University, Novosibirsk, Russian Federation
*Correspondence: voronena93@mail.ru

Abstract. This work investigates the Hall effect in n- and p-doped germanium samples through experimental measurements of Hall voltage, electrical conductivity, charge carrier mobility, and carrier concentration under varying magnetic fields and temperatures. The experimental setup involved measuring Hall voltage as a function of control current, magnetic field induction, and temperature using a TSE Co, LTD company Hall-effect unit. The linear dependence of the Hall voltage on the magnetic field was confirmed, yielding regression line slopes of $b = 0.144$ VT^{-1} $\pm$ 0.004 VT^{-1} for n-germanium and $b = 0.125$VT^{-1} $\pm$ 0.003VT^{-1} for p-germanium. Corresponding Hall constants were calculated as $R_H = 4.8 \times 10$ m^{-3}/C and $R_H = 4.17 \times 10$ m^{-3}/C. Electrical conductivities were determined as $\sigma = 53.6$ S/m for n-germanium and $\sigma = 57.14$ S/m for p-germanium. The Hall mobilities were found to be $\mu_H = 0.257 \pm 0.005$ m^2/Vs for n-germanium and $\mu_H = 0.238 \pm 0.005$ m^2/Vs for p-germanium. Carrier concentrations were $n = 13.0 \times 10^{20}$ m^{-3} for electrons and $p = 14.9 \times 10^{20}$ m^{-3} for holes. From temperature-dependent measurements, the energy bandgaps were calculated as $E_g = 0.50 \pm 0.04$ eV for n-germanium and $E_g = 0.72 \pm 0.03$ eV for p-germanium. The experimental findings provide comprehensive insights into the electronic properties of doped germanium, highlighting its behavior under magnetic fields and varying temperatures, with precise parameter evaluation crucial for semiconductor applications.

Keywords: hall effect, germanium, charge carrier mobility, electrical conductivity, semiconductor properties.

1. Introduction

The Hall effect is a crucial phenomenon in semiconductor physics, offering deep insights into the electrical properties of materials, particularly the behavior of charge carriers in the presence of a magnetic field [1]. When a current flows through a conducting material placed in a perpendicular magnetic field, a transverse voltage is generated across the material, which is proportional to the magnetic field and the current [2]. This effect is widely used to determine key material properties such as charge carrier concentration, carrier mobility, and the type of charge carriers, making it an indispensable tool for the characterization of semiconductors.

In semiconductor materials, the Hall effect allows for the differentiation between n-type and p-type conduction [3]. N-type semiconductors are characterized by an excess of electrons as the majority charge carriers, while p-type semiconductors feature holes (missing electrons) as the majority carriers. Germanium (Ge), a Group IV semiconductor, is of particular interest due to its relatively narrow bandgap of 0.66 eV and high charge carrier mobility, which makes it ideal for high-speed electronic devices, infrared detectors, and optoelectronic applications [4].

The Hall effect is instrumental in deriving several critical parameters of doped germanium, such as carrier concentration and mobility [5]. Through precise measurements of Hall voltage as a function of both the magnetic field and temperature, one can also estimate the energy bandgap and other electronic properties of the material [6]. Temperature-dependent Hall measurements provide

valuable data on both intrinsic and extrinsic conduction mechanisms in germanium, which are essential for understanding how charge carriers behave under different environmental conditions [7].

The purpose of this experiment is to study the Hall effect in n- and p-Germanium, including determining the concentration and mobility of charge carriers, as well as determining their type. To achieve this goal, the Hall voltage is measured, which occurs when an electric current passes through semiconductor wafers in a magnetic field of various inductions. The experimental data obtained are used to calculate the key parameters of semiconductors and analyze differences in their behavior under conditions of an external magnetic field. By conducting temperature- and magnetic-field-dependent measurements, this research will offer critical insights into the electronic properties of germanium, contributing to its continued optimization for use in modern semiconductor technologies.

2. Methods

The object of research was germanium, which has a diamond-type crystal structure with a cubic lattice in which the atoms are connected by covalent bonds that determine its semiconductor properties. Its bandgap width is about 0.66 eV at room temperature, which is much smaller than that of silicon, making its charge carriers - electrons and holes - highly mobile [4]. Due to its semiconductor properties, germanium has found a wide range of applications in research and technological development [8]. In semiconductor physics it serves as a model material for studying the zone structure, mobility of charge carriers and other parameters important for describing transport phenomena [5]. In the electronics industry, germanium is used to produce transistors, diodes, photovoltaic cells, and infrared sensors [9]. Its high electron mobility makes it ideal for creating high-frequency devices [10]. In optoelectronics, germanium is used in photodetectors and infrared systems due to its ability to effectively absorb infrared radiation [11].

In the pure state, germanium is an intrinsic semiconductor in which the concentrations of electrons and holes are equal. However, due to the doping process, its electrical properties can be significantly changed by introducing impurity atoms into the crystal lattice. The addition of Group V elements (e.g., phosphorus or arsenic) produces an n-type semiconductor in which the main charge carriers are electrons and the non-main charge carriers are holes. This is due to the presence of an extra valence electron in the impurities, which becomes a free charge carrier, increasing the electrical conductivity of the material. In the case of doping with Group III elements (such as boron or indium), a p-type semiconductor is formed, where the main charge carriers are holes, resulting from the lack of one electron in the valence shell of the impurity atoms. In this work, we used $1 \cdot 10^{-3}$ m thick samples.

In addition, research in the field of quantum electronics shows that germanium can be used to create quantum dots and develop new technologies in the field of quantum computing. However, all its properties are not fully understood. In connection with this, it was decided to study the semiconductor properties of germanium through the Hall effect.

The experimental technique for studying the Hall effect in p-Ge and n-Ge semiconductors involves the use of specialized TSE Co, LTD company equipment, including the installation of the Hall effect HU 2 11801-01, a digital teslameter with a tangential Hall sensor, a digital multimeter, a voltage-controlled power supply, a coil with a number of turns 600, a U-shaped iron core with pole tips, and there are also circuit boards with p-Ge and n-Ge semiconductor wafers. The equipment wiring diagram is presented in Figure 1. Additionally, a tripod, angle clamps, support rods and connecting wires are used.

Before starting the experiment, the coil is mounted on an iron core with pole tips, which are fixed on a tripod. The coil is connected to a power source to create a magnetic field. A digital multimeter measures the current flowing through the coil, and the magnetic field induction is determined using a digital teslameter. The semiconductor wafer is fixed on the Hall effect installation and connected to a power source that creates an electric current, as well as to a multimeter for measuring the Hall voltage.
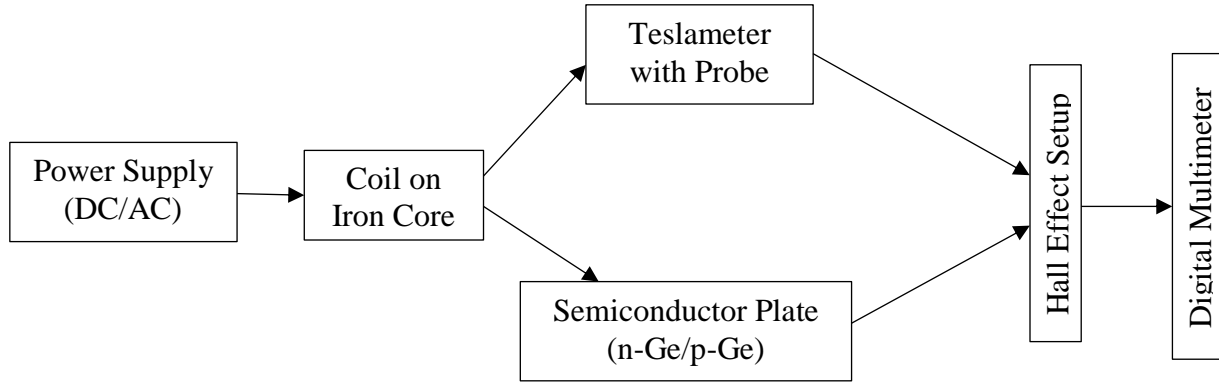
Figure 1 – Equipment wiring diagram

During the experiment, an electric current is supplied through the coil, creating a magnetic field, the magnitude of which is controlled by a teslameter. Then an electric current is passed through the semiconductor wafer, and the Hall voltage value is recorded by a multimeter. Measurements are carried out at different values of magnetic field induction and currents through a semiconductor. Similar operations are performed for both p-Ge and n-Ge semiconductors, which makes it possible to determine the type of main charge carriers and compare the results obtained.

The processing of experimental data includes the calculation of the Hall voltage according to the Equation (1):

$$U_H = \frac{BI}{ned} \tag{1}$$

Where: B – the induction of a magnetic field, I – the current through the plate, n – the concentration of charge carriers, e – the electron charge, d – the thickness of the semiconductor plate. The mobility of charge carriers is defined as:

$$\mu = \frac{U_H}{BI} \tag{2}$$

The analysis of experimental data allows us to draw conclusions about the concentration and mobility of charge carriers in the studied samples, as well as to establish differences in the behavior of p-Ge and n-Ge in the magnetic field. Moreover, the following statistical methods are used to confirm the reliability of the experimental data in the study of the Hall effect:

$$\overline{x} = \frac{1}{N}\sum_{i=1}^{N} x_i \tag{3}$$

Where: N – the number of measurements, x_i – values of individual measurements.
An estimate of the scatter of the data relative to the mean was defined as:

$$\sigma = \sqrt{\frac{1}{N-1}\sum_{i=1}^{N}(x_i - \bar{x})^2} \tag{4}$$

Graphical representations were constructed considering the statistical processing methods to confirm the results' reliability.

In order to study the dependence of the electrical characteristics of a semiconductor sample (n- or p-germanium) on temperature, the voltage changes at constant control current during heating and subsequent cooling of the sample was investigated. In this case, the current was set at 30 mA with the magnetic field off. The sample was heated to a maximum temperature of about 140 °C, after which heating was automatically stopped. After the heating was turned off, cooling curve measurements were made, recording the voltage changes as a function of sample temperature from 140 °C to room temperature.

3. Results and Discussion

During the experiment, the multimeter was connected to the Hall voltage measurement connectors on the front side of the experimental module. The module display was set to the current display mode. The current was set to zero before starting the measurements, after which the Hall

voltage was calibrated to eliminate possible initial offsets. The magnetic field was set at 250 mTl by adjusting the voltage and current of the power supply. To investigate the dependence of Hall voltage on current in n-type and p-type semiconductors, measurements were carried out at varying the current in the range from -30 mA to 30 mA with a step of 5 mA. As a result, typical dependencies were obtained as shown in Figures 2 and Figure 3 for n-germanium and p-germanium, respectively. The measured values reflect the linear dependence of Hall voltage on current.
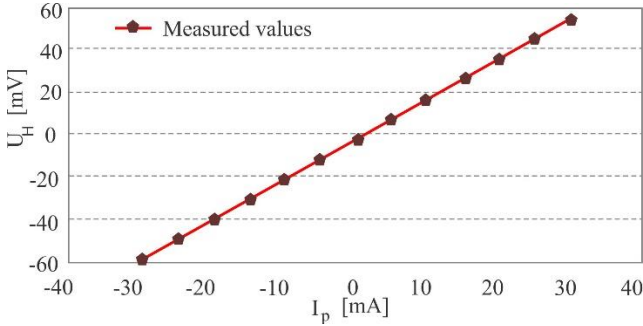

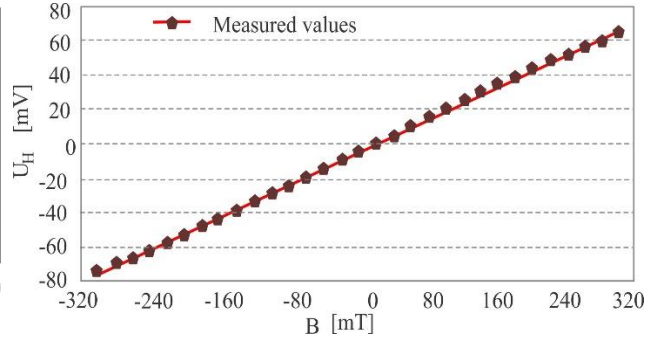Figure 2 – Hall voltage as a function of the current I_P with B = 250 mT and T = 300 K, a case for n-Germanium

Figure 3 – Hall voltage as a function of the current I_P with B = 250 mT and T = 300 K, a case for p-Germanium

Figures 2 and 3 show the linear relationship between Hall voltage and control current for both n-germanium and p-germanium. This dependence can be described by Equation (5):

$$U_H = \alpha * I_P \tag{5}$$

Where: α – is the proportionality coefficient. Since electrons are the main charge carriers in n-germanium and holes are the main charge carriers in p-germanium, the sign of the proportionality coefficient is as follows α is reversed. This leads to different directions of Hall voltage variation with increasing control current, which is clearly demonstrated by the plots in Figures 2 and 3. Thus, the sign of the Hall voltage makes it possible to determine the type of conductivity of the material.

To investigate the dependence of the sample voltage on magnetic induction, measurements were carried out when the magnetic induction varies B in the range from 0 to 300 mTl with positive field direction.

Based on the obtained data, the change in resistance of the samples was calculated using Ohm's law and the relationship between the measured voltage and the applied current. The results of the calculations were presented as plots of resistance versus magnetic induction, as shown in Figures 4 and 5.

Figure 4 – Change of resistance as a function of the magnetic flux B with I_P = 30 mA and T = 300 K for n-Germanium
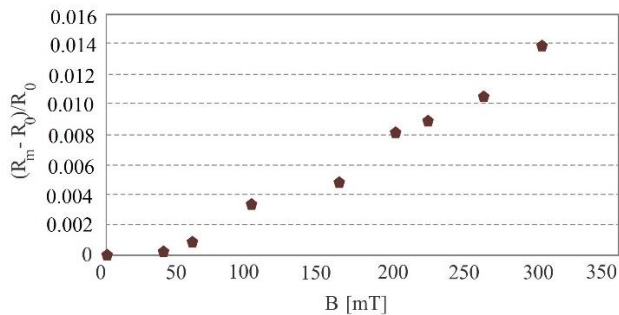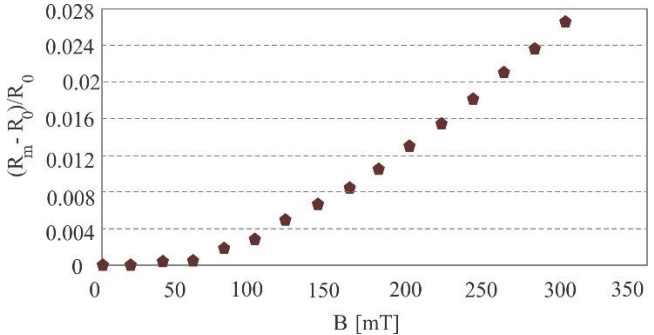

Figure 5 – Change of resistance as a function of the magnetic flux B with I_P = 30 mA and T = 300 K for p-Germanium

The obtained dependences demonstrate the influence of the magnetic field on the resistance of semiconductors, which corresponds to theoretical ideas about the behavior of charge carriers in a magnetic field.

Figures 4 and 5 show the variation of resistance for n-germanium and p-germanium samples, respectively. The graphs show a nonlinear increase in resistance with increasing magnetic induction. For n-germanium, this is due to negatively charged electrons as the main charge carriers, while for p-germanium it is due to positively charged holes. The difference in behavior is due to differences in the effective masses and mobility of charge carriers in these materials. Change of sample resistance under the action of magnetic field B is caused by a decrease in the average free path of charge carriers. When a magnetic field is applied to a semiconductor, the charge carriers begin to move along curvilinear trajectories due to the Lorentz force, which increases the probability of collisions and reduces their mobility. This leads to an increase in the effective resistance of the sample.

To study the effect of temperature on the electrical properties of a semiconductor sample, voltage changes at a constant reference current of 30 mA were investigated during heating to 140°C and cooling to 23°C of the sample. The results are presented in Figure 6a and Figure 6b.

In the intrinsic conductivity region, the electrical conductivity of a semiconductor depends on temperature and is described by an exponential dependence. The conductivity is determined by the pre-exponential coefficient, which depends on the material properties, and the forbidden zone energy, which characterizes the difference between the valence and conducting zones.
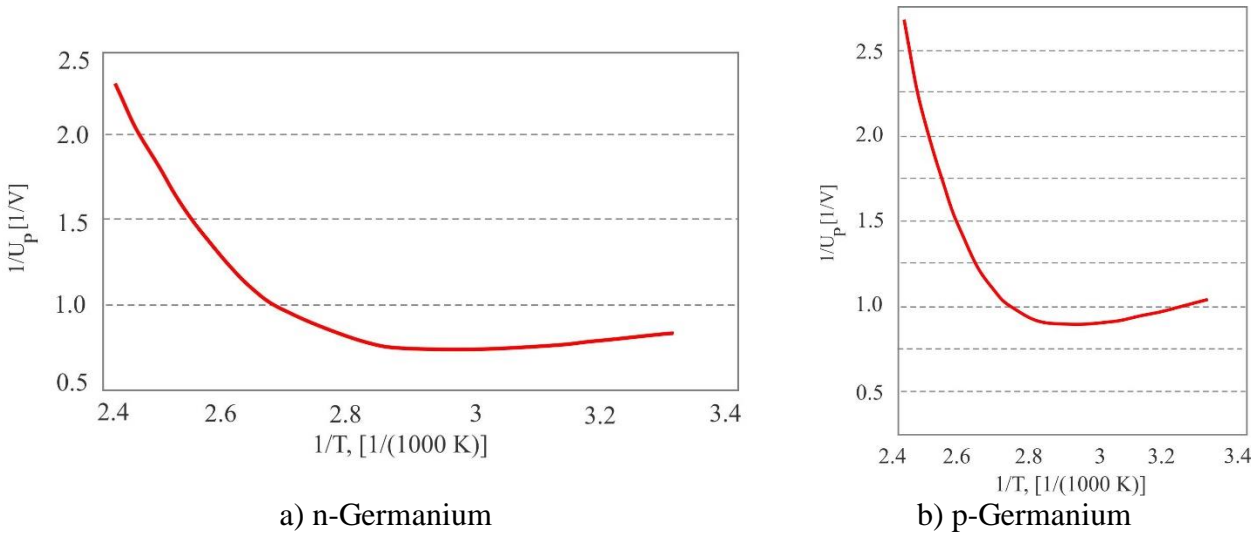

a) n-Germanium b) p-Germanium

Figure 6 – Plotting of reciprocal sample voltage with no magnetic flux and reciprocal absolute temperature $\frac{1}{T}$ with $I_P = 30$ mA

If we take into account that the conductivity decreases with increasing temperature, we can plot the dependence of the logarithm of the conductivity on the inverse temperature. This dependence will be linear, and the slope of the resulting straight line will be related to the width of the forbidden zone. Having measured the slope, we calculated the energy value of the forbidden zone using the known value of the Boltzmann constant. From the measured values presented in Figure 6a and Figure 6b, it follows that the slopes of the regression lines for n-germanium and p-germanium semiconductors are as follows $b = -2.87 \times 10^3 \text{K} \pm 0.3 \times 10^3 \text{K}$ for n-germanium and $b = -4.18 \times 10^3 \text{K} \pm 0.07 \times 10^3 \text{K}$ for p-germanium. These values confirm the temperature dependence of the conductivity in the intrinsic conduction region and allow us to estimate the bandgap width for both types of germanium with high accuracy. Thus, the bandgap width amounted to $E_g = b * 2k = (0.5 \pm 0.04)$ eV for n-germanium and $E_g = b * 2k = (0.72 \pm 0.03)$ eV for p-germanium.

The conductivity of a semiconductor sample at room temperature is calculated from its geometric dimensions and electrical resistance. The length of the sample l, its cross-sectional area A and the measured resistance R are related as follows:

$$\sigma_0 = \frac{l}{R \cdot A} \tag{5}$$

In our case, under the conditions that $l = 0.02$ m, $R = 37.3\ \Omega$ for n-Ge, and $R = 35.5\ \Omega$ for p-Ge, A = $1 \cdot 10^{-5} m^2$, the conductivity $\sigma_0 = 53.6\ \Omega^{-1} m^{-1}$ for n-Ge and $\sigma_0 = 57.14\ \Omega^{-1} m^{-1}$ for p-Ge. The Hall mobility of charge carriers has been established as $\mu_H = 0.257 \pm 0.005\ \frac{m^2}{Vs}$ and $\mu_H = 0.238 \pm 0.005\ \frac{m^2}{Vs}$ for n-Ge and p-Ge, respectively.

Next, we studied the Hall voltage relationships as a function of changes in magnetic induction and analyzed the properties of semiconductors in the presence of an external magnetic field. The results presented in Figure 7a and Figure 7b, illustrate the dependence of Hall voltage on magnetic induction for a semiconductor material at a fixed value of current 30 mA.
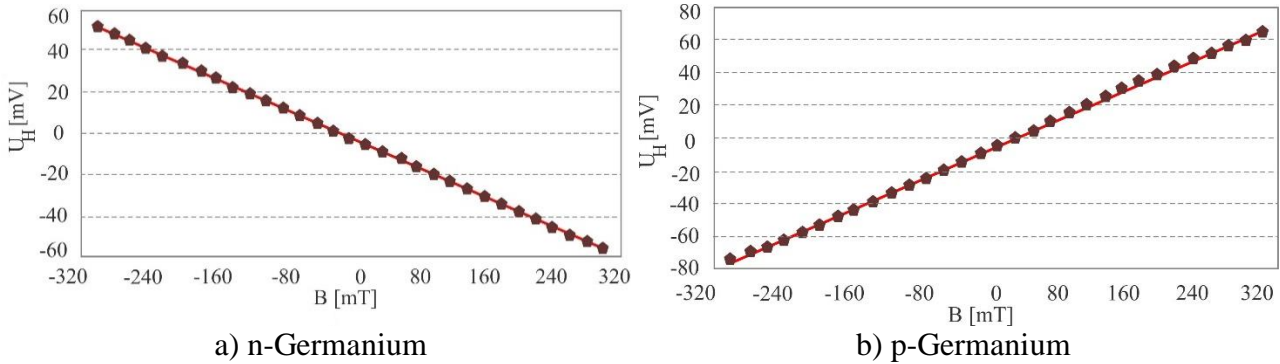

a) n-Germanium b) p-Germanium

Figure 7 – U_H as a function of magnetic flux B with T = 300 K and $I_P = 30$ mA

U_H measurements were performed as a function of magnetic induction starting from -300 mTL to 300 mTL. The polarity of the power supply coil was varied to change the direction of the magnetic field, and the magnetic induction was increased in steps of about 20 mTl. At the zero point of magnetic induction, the polarity of the field was also changed.

At a certain direction of the control current and the external magnetic field, the charge carriers in the sample are deflected towards its leading edge as a result of the Lorentz force. This deflection results in a potential difference known as the Hall voltage. In the case of an n-doped sample, the main charge carriers are electrons, so the leading edge of the sample becomes negatively charged. In a p-doped sample, the main carriers are holes, resulting in a positive charge at the leading edge.

The conductivity of the material, the mobility of charge carriers and their concentration are related to each other through the Hall constant, which is determined experimentally. Figure 7 shows the linear dependence of the Hall voltage on the magnetic induction B, which confirms the theoretical model. For the conditions used in the experiment, a regression line with the corresponding Equation 5 describing this dependence was constructed. The obtained results demonstrate the correct behavior of Hall voltage in semiconductor samples and confirm the effectiveness of the measurement method.

The experimental data presented in Figure 7, demonstrate the linear dependence of Hall voltage on magnetic induction described by Equation (6):

$$U_H = U_0 + b * B \tag{6}$$

The slope of the regression line calculated by us was $b = 0.144$ VT^{-1} with a standard deviation of ± 0.004 VT^{-1} for n-doped germanium and $b = 0.125$ VT^{-1} with a standard deviation of ± 0.003 VT^{-1} for p-doped germanium. Based on these values, the Hall constant was calculated using the Equation (7):

$$R_H = \frac{U_H}{B} \cdot \frac{d}{I} = b \cdot \frac{d}{I} \tag{7}$$

Thus, the Hall constant evaluated $R_H = 4.8 \cdot 10^{-3}\ \frac{m^3}{As}$ with standard deviation $\pm 0.2 \cdot 10^{-3}\ \frac{m^3}{As}$ for n-doped germanium and $R_H = 4.17 \cdot 10^{-3}\ \frac{m^3}{As}$ with standard deviation $\pm 0.08 \cdot 10^{-3}\ \frac{m^3}{As}$ for p-doped germanium.

The experimental results allowed us to determine the concentration of charge carriers in the studied semiconductor samples on the basis of experimentally obtained values of Hall constant. For p-doped germanium the concentration of holes p, calculated by Equation (8):

$$p = \frac{1}{e} \cdot R_H \tag{8}$$

And amounted to $p = 14.9 \cdot 10^{20} \ m^{-3}$. Similarly, for n-doped germanium, the electron concentration calculated by the same Equation is $n = 13.0 \cdot 10^{20} \ m^{-3}$. The obtained results demonstrate the effectiveness of the method of measuring the parameters of charge carriers using the Hall effect.

4. Conclusions

During the experiment, a linear increase in the Hall voltage was obtained with an increase in the magnetic field. The slopes of the regression lines were $b = 0.144$ VT^{-1} with a standard deviation of ± 0.004 VT^{-1} for n-doped germanium and $b = 0.125$ VT^{-1} with a standard deviation of ± 0.003 VT^{-1} for p-doped germanium. These values made it possible to calculate the Hall constants $R_H = 4.8 \cdot 10^{-3} \frac{m^3}{As}$ with standard deviation $\pm 0.2 \cdot 10^{-3} \frac{m^3}{As}$ for n-doped germanium and $R_H = 4.17 \cdot 10^{-3} \frac{m^3}{As}$ with standard deviation $\pm 0.08 \cdot 10^{-3} \frac{m^3}{As}$ for p-doped germanium.

The calculated conductivity of the samples at room temperature was $\sigma_0 = 53.6$ Ω^{-1}m^{-1} for n-Ge and $\sigma_0 = 57.14$ Ω^{-1}m^{-1} for p-Ge. Based on these values, the Hall mobility of charge carriers was determined as $\mu_H = 0.257 \pm 0.005 \frac{m^2}{Vs}$ and $\mu_H = 0.238 \pm 0.005 \frac{m^2}{Vs}$ for n-Ge and p-Ge, respectively. The electron concentration was $n = 13.0 \cdot 10^{20} \ m^{-3}$ for n-Ge and the concentration of holes $p = 14.9 \cdot 10^{20} \ m^{-3}$ was for p-germanium. As a result, of temperature measurements, the values of the forbidden band width were determined as $Eg = 0.50 \pm 0.04$ eV for n-germanium and Eg=0.72±0.03eV for p-germanium. The nonlinear increase in resistance with increasing magnetic field recorded in Figures 4 and 5, confirmed the decrease in the mean free path of charge carriers. Thus, the experimental results fully reflect the electrical characteristics of the studied samples.

References

[1] R. A. Masut, "Poisson's equation in semiconductors: impact of charge depletion on Hall effect measurements," *Can. J. Phys.*, vol. 101, no. 3, pp. 141–149, Mar. 2023, doi: 10.1139/cjp-2022-0158.

[2] N. Saleh and A. H. Qureshi, "Conductivity tensor and hall effect in magnetic semiconductors," *J. Appl. Phys.*, vol. 42, no. 11, pp. 4313–4314, Jan. 1971, doi: 10.1063/1.1659772.

[3] T. Bauer, J. Kolb, A. B. Hummel, H. G. Roskos, Y. Kosevich, and K. Köhler, "Coherent hall effect in a semiconductor superlattice," *Phys. Rev. Lett.*, vol. 88, no. 8, pp. 86801/1-86801/4, Feb. 2002, doi: 10.1103/PhysRevLett.88.086801.

[4] C. A. Stephenson *et al.*, "Band structure of germanium carbides for direct bandgap photonics," *2016 IEEE Photonics Soc. Summer Top. Meet. Ser. SUM 2016*, pp. 53–54, Aug. 2016, doi: 10.1109/PHOSST.2016.7548543.

[5] M. M. Dettling *et al.*, "Carrier mobilities in heavily doped pseudomorphic Ge1-x Snx-epilayers," *2020 43rd Int. Conv. Information, Commun. Electron. Technol. MIPRO 2020 - Proc.*, pp. 17–21, Sep. 2020, doi: 10.23919/MIPRO48935.2020.9245273.

[6] X. Li *et al.*, "Optical bandgap anomaly with tuning dimensionality in germanium perovskites: Interplay between quantum confinement and lone pair expression," *Chem*, vol. 10, no. 3, pp. 891–909, Mar. 2024, doi: 10.1016/j.chempr.2023.11.011.

[7] M. A. Razali, A. J. Smith, C. Jeynes, and R. M. Gwilliam, "Temperature-dependant study of phosphorus ion implantation in germanium," *AIP Conf. Proc.*, vol. 1496, pp. 193–196, Jan. 2012, doi: 10.1063/1.4766522.

[8] J. Satgé, "Some applications of germanium and its derivatives," *Main Gr. Met. Chem.*, vol. 27, no. 6, pp. 301–307, Jan. 2004, doi: 10.1515/MGMC.2004.27.6.301.

[9] K. Li, K. H. Kong, H. Gamble, and M. Armstrong, "Ultra-shallow emitter formation for germanium bipolar transistor by diffusion from polycrystalline germanium," *2011 Int. Semicond. Device Res. Symp. ISDRS 2011*, p. 2011, doi: 10.1109/ISDRS.2011.6135275.

[10] M. Mederos, S. N. M. Mestanza, R. Lang, I. Doi, and J. A. Diniz, "Germanium nanoparticles grown at different deposition times for memory device applications," *Thin Solid Films*, vol. 611, pp. 39–45, Jul. 2016, doi: 10.1016/j.tsf.2016.05.026.

[11] K. L. Guo, H. H. Chen, X. M. Huang, T. H. Hu, and H. Y. Liu, "Solar broadband metamaterial perfect absorber based on dielectric resonant structure of Ge cone array and InAs film," *Chinese Phys. B*, vol. 30, no. 11, p. 114201, Jan. 2022, doi: 10.1088/1674-1056/abf91e.

Information about authors:

Galina Troshina – Candidate of Physical and Mathematical Sciences, Researcher at Interdisciplinary Center for Particle Physics and Astrophysics, Novosibirsk State University, Novosibirsk, Russian Federation, g.n.troshina@mail.ru

Natalya Voronena – MS, Research Assistant at Interdisciplinary Center for Particle Physics and Astrophysics, Novosibirsk State University, Novosibirsk, Russian Federation, voronena93@mail.ru

Author Contributions:

Galina Troshina – concept, interpretation, methodology, resources, data collection, editing.
Natalya Voronena – testing, modeling, analysis, visualization, drafting, funding acquisition.

Conflict of Interest: The authors declare no conflict of interest.

Use of Artificial Intelligence (AI): The authors declare that AI was not used.

Article

Spectroscopic analysis of α-particle emission from ^{241}Am and ^{226}Ra sources

Tatiana Timoshinova, Alexander Afanasyev*

Department of Nuclear Physics, Voronezh State University, Voronezh, Russian Federation
*Correspondence: afanasyev.alex15@yandex.ru

Abstract. This paper investigates the energy spectra of α-particles emitted by radioactive sources ^{241}Am and ^{226}Ra using a multichannel analyzer. Calibration of the detection system was performed with the primary peak of 241Am at 5486 keV, yielding a sensitivity of $S = 0.4631$ mV/keV. The energy dependence on channel number was established, ensuring accurate energy characterization of the measured spectra. The effect of air pressure on α-particle spectra was analyzed by varying the pressure from vacuum to 500 hPa and 1000 hPa. Results demonstrated a systematic shift of the main peak position towards lower channels due to energy losses in the air, accompanied by peak broadening. For ^{241}Am, the primary peak shifted from approximately channel 2500 in vacuum to channels 2200 and 2000 at 500 hPa and 1000 hPa, respectively. The peak broadening increased linearly with energy loss, described by the relationship $q = 0.073 \cdot \Delta E + 24.2$ keV, where the constant 24.2 keV represents the intrinsic resolution of the detector. Comparative analysis of ^{241}Am and ^{226}Ra spectra revealed the simpler structure of ^{241}Am, characterized by a single primary peak, versus the more complex, multi-component spectrum of ^{226}Ra, which reflects contributions from daughter nuclides. Despite this complexity, the detector successfully captured the overall profile of ^{226}Ra. These findings confirm the high precision of the detection system in measuring α-particle spectra under varying experimental conditions and highlight its potential for further studies of α-radiation interactions and the development of advanced detector technologies.
Keywords: α-particle spectroscopy, radioactive sources, energy loss in the air, detector calibration, peak broadening.

1. Introduction

α-particle emission and its interactions with matter play a pivotal role in understanding nuclear decay processes and the fundamental principles of radiation detection. α-particles, which are helium nuclei emitted during the decay of certain radionuclides, exhibit strong interactions with matter due to their positive charge [1]. As a result, their range in materials is limited to a few centimeters in air or micrometers in condensed matter. The theoretical framework for α-particle interactions, including energy loss mechanisms, is well-documented in nuclear physics [2], [3].

One of the key characteristics of α-particles is their energy loss as they traverse matter [4]. This loss is primarily governed by interactions with electrons in the material, leading to a decrease in particle energy that is approximately proportional to the particle's path length or the electron density of the medium. Such proportionality is particularly valid for α-particles with initial energies exceeding 2.8 MeV [5]. However, additional factors, such as the physical configuration of the radioactive source and the presence of encapsulating materials, can significantly influence the energy spectrum observed by a detector.

The decay chain of ^{226}Ra provides a unique opportunity to examine these effects [6]. Radium-226 is typically in radioactive equilibrium with its decay products up to ^{210}Po, which has a half-life of 22.3 years [7]. However, depending on the age of the source, equilibrium may not extend to later decay products, such as ^{210}Po. In such cases, the fraction of ^{210}Po present in the source may be reduced, leading to the absence or attenuation of its characteristic peak in the observed spectrum. By analyzing the relative intensities of peaks associated with ^{210}Po and neighboring nuclides, it is

possible to estimate the production date of the radioactive source. For ^{226}Ra, several α-particle emissions are expected to appear in the spectrum, including peaks at 4784 keV (^{226}Ra), 5304 keV (^{210}Po), 5489 keV (^{222}Rn), 6002 keV (^{218}Po), and 7687 keV (^{214}Po) [7]. These peaks represent the contributions of different decay products within the radium series.

Similarly, ^{241}Am, which decays exclusively to stable ^{237}Np, emits α-particles with a predominant energy of 5486 keV in 85% of its decays (Figure 1) [8]. This emission serves as a calibration point for the energy scale and provides a benchmark for comparison with the more complex spectrum of ^{226}Ra.

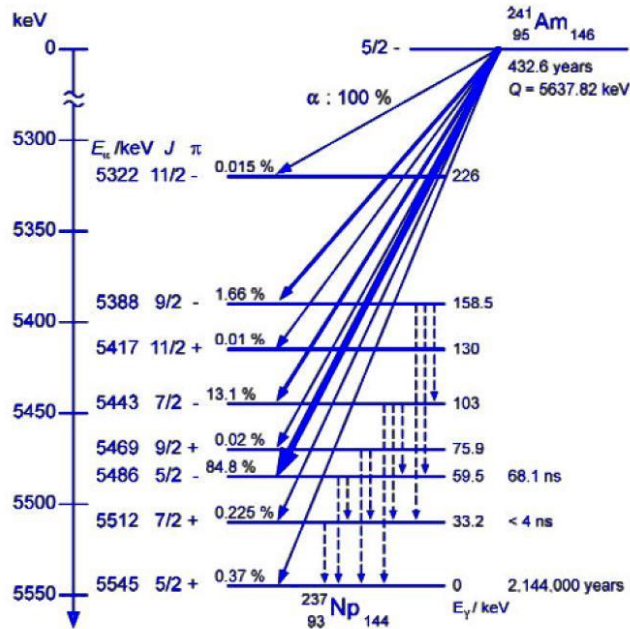Figure 1 – ^{241}Am decay diagram [8]

While numerous studies have investigated α-particle spectra and energy loss mechanisms, certain limitations persist. Earlier research [9], [10] often focused on idealized scenarios where α-emitting radionuclides were assumed to reside in infinitely thin layers or sources with uniform radionuclide distributions. These assumptions oversimplify the actual conditions of encapsulated sources, where the presence of non-uniform material layers and varying source thicknesses significantly affect energy loss and spectral broadening.

Moreover, many studies [11], [12] did not adequately address the combined effects of encapsulation and radionuclide distribution depth. The encapsulation layers were often treated as uniform barriers, overlooking the variability in material composition and thickness. This oversight can lead to inaccuracies in interpreting spectral features, particularly in determining mean energy losses and the associated peak shifts.

Additionally, past research [13] has frequently neglected the implications of radioactive disequilibrium within decay chains, particularly for long-lived nuclides. The absence or attenuation of certain decay products due to source age or manufacturing variations was not systematically incorporated into spectral analyses. As a result, the potential to estimate source production dates based on peak intensity ratios remains underexplored.

In this regard, this work aims to address these limitations by systematically investigating the effects of encapsulation layers and radionuclide distribution depth on α-particle spectra. The main aspects are developing a comprehensive understanding of peak broadening and energy loss mechanisms due to encapsulation and material composition; and establishing a methodology to analyze the spectral contributions of decay products in radioactive equilibrium. Also, estimating the production date of radioactive sources by comparing peak intensity ratios, particularly for ^{226}Ra. The findings of this study hold significant value for nuclear physics, radiation safety, and material

characterization. By addressing the gaps in prior research and providing a detailed analysis of spectral features, this work contributes to enhancing the accuracy of α-particle detection systems and advancing the field of α spectroscopy.

2. Methods

In the present paper, α-particle emissions from ^{226}Ra and ^{241}Am sources were investigated, considering the effects of source encapsulation and radionuclide distribution within the material. Encapsulation layers, commonly used to isolate radioactive sources, introduce notable changes to the observed spectra. All α-particles emitted from the ^{226}Ra source must pass through the encapsulating layer before reaching the detector [14]. This interaction results in energy loss proportional to the thickness of the covering, which in turn causes peak broadening in the detected energy spectrum. Since all particles encounter the same layer, the mean energy loss can be considered uniform.

However, encapsulation is not the sole factor influencing the observed spectra. The radionuclides within the ^{226}Ra source are distributed over a finite thickness of the source material rather than being confined to a thin surface layer. Consequently, α-particles emitted from varying depths encounter different material thicknesses, resulting in additional energy loss and contributing further to the broadening of the detected peaks. The combined effects of encapsulation and radionuclide distribution require careful consideration to accurately interpret the observed spectral features.

The following equipment was used in this experiment to investigate the α-energy of the ^{226}Ra isotope using a multichannel analyzer (MCA). A container for nuclear physics experiments, an α- and photo detector, a preamplifier for the α detector, a MCA from Gulmay Company, special software, a 220V two-stage diaphragm pump, a DVR 2 pro vacuum gauge with a measurement range of 1 to 1000 hPa, two NBR vacuum tubes 6/14 mm in size and 1 m long each, a Y-tube connector with an inner diameter of 8-9 mm, a 20 mm wide socket, an ^{241}Am radioactive source with an activity of 3.7 kBq, a ^{226}Ra radioactive source with a maximum activity of 4 kBq, and a 750 mm long shielded BNC cable. The schematic connection block is shown in Figure 2.
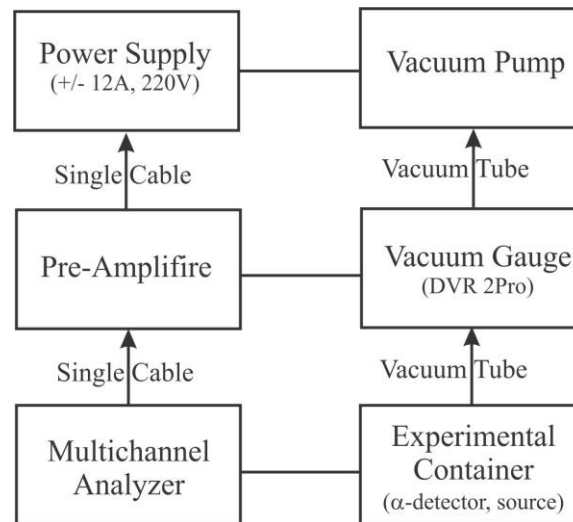
Figure 2 – Equipment wiring diagram

The black shield was mounted on the detector, after which the detector itself was attached to the flange cover. The uncovered ^{241}Am source was placed into the black shield of the detector as far as it would go, ensuring a minimum distance between the source and the sensitive area of the detector. The retractable rod was retracted and secured with a milled screw, ensuring a stable position of the source relative to the detector. The flanged cover with the detector mounted was mounted on the experimental container, ensuring a tight connection. The counting rate selected 50 – 60 per second.

A diaphragm pump created a vacuum in the experimental container, the level of which was monitored using a DVR 2 pro vacuum gauge. Vacuum tubing connected via a Y-connector and socket provided a reliable vacuum connection, minimizing air leaks. These measures contributed to the stable experimental conditions necessary to accurately measure the alpha spectra of the ^{226}Ra isotope using the multichannel analyzer.

The registration of the α-radiation spectrum from the uncovered ^{241}Am source with an energy of 5.486 MeV was used to calibrate the measuring equipment, which ensured high accuracy and reproducibility of the results. Calibration at this peak is an important step because it allows a correct interpretation of the data obtained during the experiment and ensures an adequate comparison of the measured values with theoretical expectations.

To further analyze α-particles of known energy, a portion of air was used as a deceleration medium. The effect of air on α-particles is to reduce the energy of the particles as they pass through this medium, resulting in a shift of the mean energy and a broadening of the peak in the energy spectrum. This phenomenon is the result of repeated collisions of particles with air molecules, during which they slow down and lose energy. The air from the vessel was brought to a pressure of 500 hPa followed by the collection of about 10000 pulses. The magnitude of the shift and broadening of the peak depends on various factors such as the density of the medium, the path length of the particles in the air, and the initial energy of the particles. To quantitatively analyze this process, the ratio of average energy loss to peak broadening was measured, and it was found that in the energy range above 2.8 MeV this ratio can be assumed to be linear. Then, with the air completely vented from the experimental vessel, the spectrum was recorded at ambient pressure (about 1000 hPa), with the source still directly in front of the detector and again collecting about 10 thousand pulses. This finding has important implications for the accurate estimation of particle energy loss in different environments and can be used to calibrate measurements in more complex environments.

In addition to analyzing the spectrum from the uncoated source, the energy spectrum of α-particles emitted from a ^{226}Ra source coated with a shielding was also recorded. In this stage, the speed was much higher and amounted to 200 – 250 pulses per second. The emission spectrum recorded using the same multichannel analyzer was evaluated to study the effect of the coating on the α-emission characteristics. The source coating has a significant effect on the energy and distribution of α-particles, as it can significantly alter both their initial energy and the path they take through the environment. Analysis of this spectrum allows a comparative study between the radiation from coated and uncoated sources, which in turn provides a better understanding of the effect of shielding materials on the radiation characteristics. This study has important implications for the development of more effective shielding techniques and for improving measurement accuracy in radiation experiments.

Thus, in this study, modern methods of recording and analyzing α-radiation spectra using a multichannel analyzer were used to obtain accurate data on radiation characteristics and to evaluate the influence of various factors, such as the deceleration medium and source coating, on the energy and distribution of α-particles.

3. Results and Discussion

When recording the α-particle spectrum, the MCR divided the input voltage range from 0 V to 4 V into 4000 equal intervals. Each interval corresponds to a specific channel, and the width of one channel is 1 mV. To adapt the measuring range, an offset function is used that shifts the entire 4-volt interval relative to a starting point specified as a percentage of the maximum voltage. For example, with an offset of 5%, the measurement interval starts at 0.2 V. In such a case, channel zero recorded pulses between 0.1995 V and 0.2005 V, and channel 3999 recorded pulses between 4.1935 V and 4.2005 V. This approach provides accurate registration of energy spectra and allows to adapt the sensitivity of the system to the given experimental conditions. All collected data are presented in Table 1.

Table 1 – Data for the ^{241}Am with x_1 position of the left side of the peak at half-max and the x_2 position of the right side of the peak at half-max

hPa, air	Peak, counts	FWHM	$\dfrac{\chi_1}{ch}$	$\dfrac{\chi_2}{ch}$	$\dfrac{(x_1 + x_2)}{2}$
11	260	11	2335	2346	2340.5
50	266	25	2144	2169	2156.5
1000	366	39	1937	1976	1956.5

The graph on Figure 3 shows the spectra of α-particles registered at different pressures of the medium. Each curve of the spectrum corresponds to a certain pressure: vacuum, 500 hPa, and 1000 hPa. The horizontal axis of the graph denotes the number of the MCR channel, which is related to the energy of the registered particles. The vertical axis represents the number of registered impulses (number of events) for each channel.
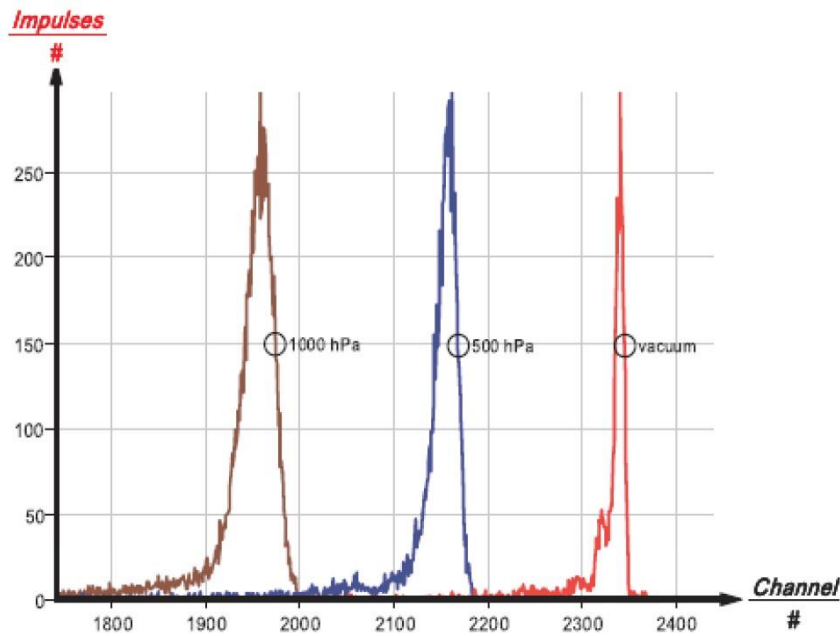
Figure 3 – Test results of ^{241}Am

Spectrum in vacuum (red curve): It is in the channel region around 2400, which corresponds to the maximum energy of the α-particles, since there is no significant deceleration in vacuum. The peak is narrow, indicating minimal broadening and high precision in recording the particle energy. Spectrum at 500 hPa (blue curve): There is a shift of the peak to lower channel numbers, around 2200, indicating a loss of α-particle energy as it passes through the pressurized medium. The broadening of the peak becomes prominent, which is due to the scattering of particles on air molecules. Spectrum at 1000 hPa (brown curve): The peak is significantly shifted to the low channel number region, around 2000, indicating an even greater particle energy loss in the denser medium. The broadening of the peak increases, which is explained by the intensification of scattering processes.

To accurately determine the energy of the α-particles detected by the multichannel analyzer, a calibration relation based on the main peak energy of 5486 keV for the ^{241}Am α-emitter was used. The sensitivity of the detector system calculated from this energy was S=0.4631mV/keV. As a calibration factor, this value allows us to determine the energy E corresponding to the channel number n, by the Equation (1):

$$E = \frac{(n+2)}{S} \tag{1}$$

The introduced coefficient correctly relates the channel numbers of the spectrum to the particle energies, providing a high estimation accuracy. Figure 4 shows the graphical dependence of the peak

width of α-particles on the average energy loss ΔE, corresponding to the data given in Table 2. The peak broadening is directly related to the energy loss of particles as they pass through the medium, which is confirmed by the experimental results.

Table 2 – A linear relationship between the average energy loss

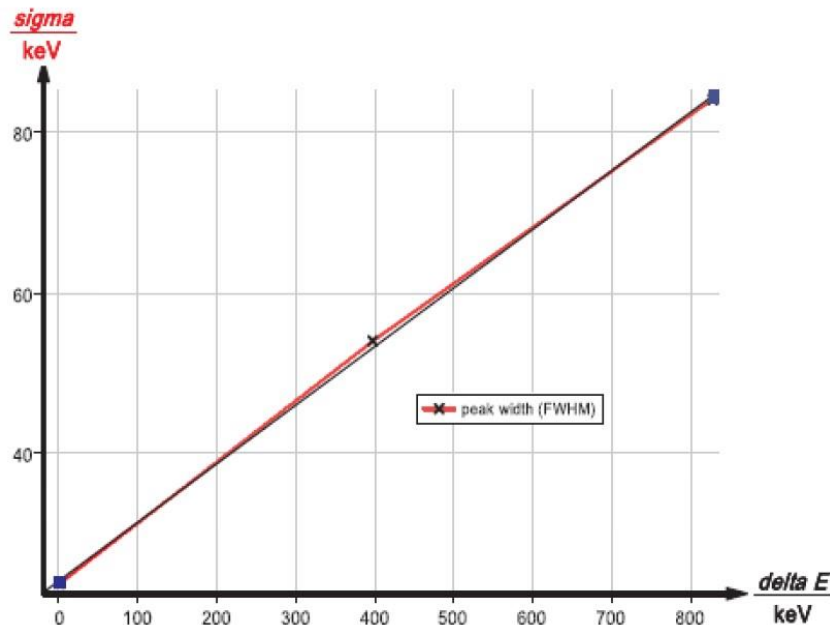| Peak ch.	Δ ch.	ΔE, keV	σ/ch.	σ, keV
2340.5	0	0	11	23.8
2156.5	-184	397.3	25	54.0
1956.5	-384	829.2	39	84.2

Figure 4 – Peak width as it relates to energy loss

Value of ΔE and peak width, especially in the energy range above 2.8 MeV. These data were obtained by measurements under different pressures (vacuum, 500 hPa, 1000 hPa). The experimental results confirm that an increase in the average energy loss leads to an increase in the peak width due to the growing contribution of scattering and braking processes.

Thus, the above dependences and graphical data confirm the high calibration accuracy and efficiency of the method for analyzing the spectra of α-particles, which is important for further studies of the interaction of high-energy particles with various media.

To describe the dependence of the peak width σ on the average energy loss ΔE, the line of best fit was calculated and expressed by the Equation (2):

$$q = 0.073 \cdot \Delta E + 24.2 \ keV \tag{2}$$

Where 24.2 keV is due to the energy resolution limit of the detector. This value characterizes the contribution of hardware resolution to the measurements and confirms the accuracy of the data obtained. The equation shows a linear dependence of the peak width on the average energy loss, which corresponds to the expected influence of scattering and inhibition of α-particles during their interaction with the medium.

Figure 5 shows the α-radiation spectrum of source [226]Ra, supplemented by the results obtained for source [241]Am. The spectrum of the [226]Ra source shows a clear structure, where four main lines corresponding to the α-decay of isotopes belonging to the radionuclide series can be distinguished. Despite the overlap of the lines, the whole profile is seen as a single composite line, which is due to the limitations of the detector resolution. The results of analyzing the spectrum of the [226]Ra source are presented in Table 3. The table contains data on peak positions (channel numbers), their widths σ, calculated energies E, and relative intensities. Comparison with the results for [241]Am allows us to

evaluate the calibration accuracy of the detector setup and to confirm its suitability for recording α-radiation spectra with high resolution.

Table 3 – Collected data of two sources ^{241}Am and ^{226}Ra

n/ch.	E, keV	Literature value, keV	Energy loss ΔE, keV	Peak displacement, channels
2897	6688	7687	999	463
2027	4809	6002	1193	552
1744	41988	5489	1291	598
1407	3470	4784	1314	608

Thus, the analysis of the spectra ^{226}Ra and ^{241}Am spectra demonstrated the agreement of experimental data with theoretical models, which confirms the high accuracy and reliability of the applied technique of α-particle registration. The Figure 5 shows a comparison of the energy spectra of α-particles recorded for two radioactive sources, ^{241}Am and ^{226}Ra, under different pressure conditions. The spectra show significant changes in the shape, position, and width of the peaks depending on the pressure of the medium and the type of radioactive emitter.
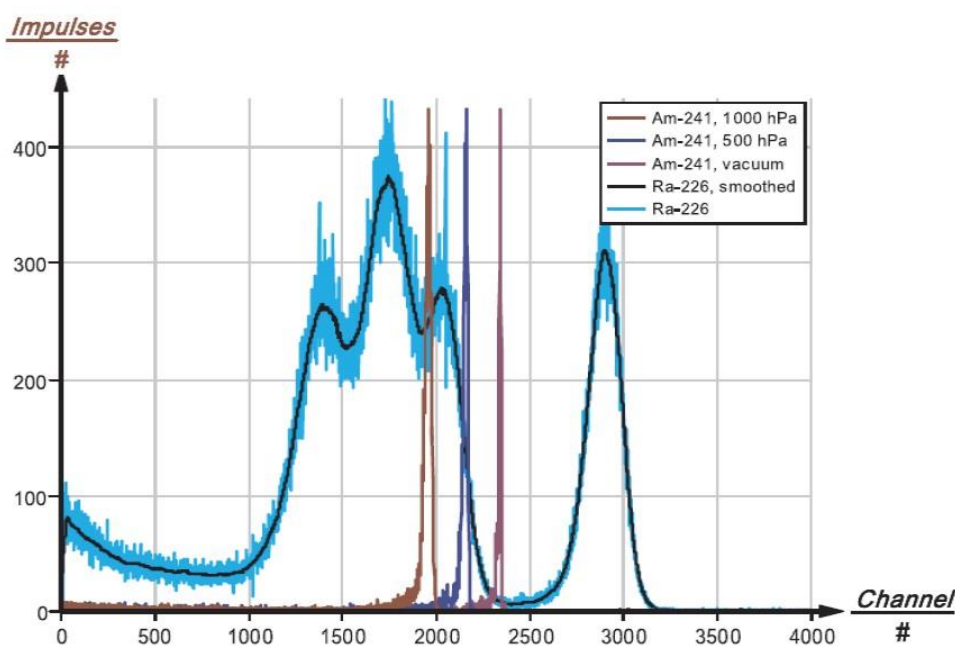

Figure 5 – ^{241}Am peak positions as a reference for the ^{226}Ra spectrum

The detailed review of spectra of ^{241}Am (curves for vacuum, 500 hPa and 1000 hPa) presents the following: at the vacuum (purple curve) the peak is at the maximum channel (around 2500), corresponding to an α-particle energy of 5486 keV recorded without deceleration in air. The shape of the peak is narrow, indicating that the influence of scattering processes is minimal. At a pressure of 500 hPa (blue curve) the peak shifts to the region of lower channel numbers (about 2200), which is due to the loss of particle energy by interaction with air molecules. The broadening of the peak increases, indicating the contribution of scattering and inhomogeneities in the medium. At a pressure of 1000 hPa (brown curve) the peak shifts even further (towards the 2000 channel) with a marked increase in width. This is due to the significant inhibition of particles in the denser medium, which increases both the average energy loss and its fluctuations.

For the source ^{226}Ra, the α-particles have a more complex spectrum including several components corresponding to different decay energies of the daughter nuclides in the radionuclide series. The spectrum includes four main lines, but due to the limited resolution of the detector the whole profile can be observed as a single composite line. The black smoothed curve is used to emphasize the general trend and shows the average energy distribution of the α-particles.

The ^{226}Ra spectrum generally occupies a lower channel region than the ^{241}Am spectrum, which is due to differences in the energies of the emitted α-particles. The broadening of the ^{226}Ra spectrum is also higher due to the contribution of daughter decay products.

This effect can be attributed to several factors. An increase in pressure leads to an increase in the number of collisions of α-particles with air molecules, which causes their inhibition. This is manifested by a shift of the peak to the region of smaller channel numbers. Also, the increasing number of collisions leads to fluctuations in energy loss, which causes the broadening of the spectrum. This dependence is linear in the energy range above 2.8 MeV, as shown earlier. These results confirm the sensitivity of the α-particle registration method to changes in experimental conditions (pressure, type of source) and demonstrate the ability of the detector system to distinguish spectra with high accuracy.

4. Conclusions

The energy spectra of α-particles emitted by ^{241}Am and ^{226}Ra radioactive sources were studied using a MCA. The measurements and analysis made it possible to characterize the influence of external conditions, such as the pressure of the medium, on the spectrum parameters and to determine the accuracy and resolution of the detector system. The main calibration source was ^{241}Am, with a main peak at an energy of 5486 keV. Based on this peak, the sensitivity of the detector system was calculated to be $S = 0.4631 \text{mV/keV}$. The obtained value was used to convert the channel numbers into energy values, which provided an accurate relationship between the measured parameters and the energy of the α-particles. Under vacuum conditions, the spectra are characterized by narrow peaks, minimal energy loss, and an exact position corresponding to the energy of the α-particles.

At pressures of 500 hPa and 1000 hPa, the α-particles lose energy by interaction with air molecules, resulting in a shift of the peaks to a region of lower channel numbers. For example, the main peak of ^{241}Am, located near the 2500th channel in vacuum, shifted to the 2200 and 2000 channels at 500 and 1000 hPa, respectively. The ^{226}Ra spectrum shows a more complex structure including several components corresponding to different α-decay energies of the daughter nuclides. Despite this, the limited resolution of the detector smooths the individual lines into a composite spectrum. The ^{241}Am spectrum is characterized by a single main peak, which makes it convenient for calibration.

It was found that the minimum peak width (24.2 keV) is due to the hardware resolution of the system, which confirms its suitability for high-precision measurements of α-particle spectra.

Thus, the investigations have shown that the technique used allows us to accurately record the energy spectra of α-particles, to analyze the influence of experimental conditions on the spectrum parameters, and to identify the main lines for various radioactive sources. The results can be used for further studies of α-radiation, including the study of the interaction of high-energy particles with various media, as well as for the development and testing of new detector systems.

References

[1] P. Schuck, H. Horiuchi, G. Röpke, and A. Tohsaki, "Alpha-particle condensation in nuclei," *Acta Phys. Hungarica New Ser. Heavy Ion Phys.*, vol. 18, no. 2, pp. 241–246, Jan. 2003, doi: 10.1556/APH.18.2003.2-4.19.

[2] T. C. Doan, J. Li, J. Y. Lin, and H. X. Jiang, "Response of alpha particles in hexagonal boron nitride neutron detectors," *Appl. Phys. Lett.*, vol. 110, no. 21, p. 213502, May 2017, doi: 10.1063/1.4984112.

[3] V. G. Kiptily *et al.*, "Observation of alpha-particles in recent D-T experiments on JET," *Nucl. Fusion*, vol. 64, no. 8, p. 086059, Aug. 2024, doi: 10.1088/1741-4326/ad5c81.

[4] "Measuring energy loss of alpha particles in different vacuum conditions-Web of Science Core Collection." Accessed: Dec. 24, 2024. [Online]. Available: https://www.webofscience.com/wos/woscc/full-record/WOS:000292674300005

[5] P. Hazdra and V. V. Komarnitskyy, "Accurate Identification of Radiation Defect Profiles in Silicon after Irradiation with Protons and Alpha-Particles in the MeV Range," *Solid State Phenom.*, vol. 95, pp. 387–392, Jan. 2004, doi: 10.4028/www.scientific.net/ssp.95-96.387.

[6] M. Mazanova, P. Dryak, and M. Havelka, "Emission probability measurement of γ- and X- rays in Ra-226 and Pb-210 decay," *Appl. Radiat. Isot.*, vol. 134, pp. 429–432, Apr. 2018, doi: 10.1016/j.apradiso.2017.10.023.

[7] D. Planaj and M. Baskaran, "Inventory-based evaluation of 210Po-210Pb-226Ra disequilibria in deep oceans and new insights on their utility as biogeochemical tracers: A global data synthesis of research over six decades," *Earth-Science Rev.*, vol. 252, p. 104759, May 2024, doi: 10.1016/j.earscirev.2024.104759.

[8] C. H. Pyeon, M. Yamanaka, T. Sano, and K. Takamiya, "Integral Experiments on Critical Irradiation of 237Np and 241Am Foils at Kyoto University Critical Assembly," *Nucl. Sci. Eng.*, vol. 193, no. 9, pp. 1023–1032, Jan. 2019, doi: 10.1080/00295639.2019.1603014.

[9] P. Tavčar, R. Jakopič, and L. Benedik, "Sequential determination of 241Am, 237Np, Pu radioisotopes and 90Sr in soil and sediment samples," *Acta Chim. Slov.*, vol. 52, no. 1, pp. 60–66, Jan. 2005.

[10] T. Tanaka *et al.*, "Migration mechanisms of 237Np and 241Am through loess media," *J. Radioanal. Nucl. Chem.*, vol. 256, no. 2, pp. 205–211, May 2003, doi: 10.1023/A:1023916829838.

[11] T. Tanaka and N. Ya-anant, "Study on migration behaviour of 237Np and 241Am in near-surface environments," *Radiat. Prot. Dosimetry*, vol. 146, no. 1, pp. 303–306, Jul. 2011, doi: 10.1093/rpd/ncr176.

[12] C. Liu *et al.*, "The migration of radionuclides 237Np, 238Pu and 241Am in a weak loess aquifer: A field column experiment," *Radiochim. Acta*, vol. 89, no. 8, pp. 519–522, Jan. 2001.

[13] R. A. Dewberry, "Calculation of 237Np and 241Am detector calibration constants from first principles," *J. Radioanal. Nucl. Chem.*, vol. 262, no. 3, pp. 783–787, Jan. 2004, doi: 10.1007/s10967-004-0511-x.

[14] N. K. Sethy, S. Singh, V. N. Jha, G. Verma, S. K. Jha, and M. S. Kulkarni, "Field Evaluation of an Encapsulated 226Ra–222Rn Source," *Mapan - J. Metrol. Soc. India*, vol. 39, no. 1, pp. 131–137, Mar. 2024, doi: 10.1007/s12647-023-00720-3.

Information about authors:
Tatiana Timoshinova – Candidate of Physical and Mathematical Sciences, Junior researcher, Department of Nuclear Physics, Voronezh State University, Voronezh, Russian Federation, tati.timosh.2007@gmail.com
Alexander Afanasyev – PhD Student, Research Assistant, Department of Nuclear Physics, Voronezh State University, Voronezh, Russian Federation, afanasyev.alex15@yandex.ru

Author Contributions:
Tatiana Timoshinova – concept, methodology, resources, data collection, testing, modeling, analysis.
Alexander Afanasyev – visualization, interpretation, drafting, editing, funding acquisition.

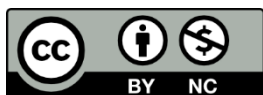**Conflict of Interest:** The authors declare no conflict of interest.

Use of Artificial Intelligence (AI): The authors declare that AI was not used.

Article

Investigation of splitting of a beam of potassium atoms in the classical Stern-Gerlach experiment at varying inhomogeneity of the magnetic field

[ID] Assel Akhmetova[*]

Laboratory of Alternative Energy and Nanotechnology, Kazakh-British Technical University, Almaty, Kazakhstan
*Correspondence: assel.akhmetova.95@bk.ru

Abstract. The splitting of a beam of potassium atoms in the classical Stern-Gerlach scheme under varying inhomogeneity of the magnetic field is experimentally investigated in this work. First, the basic shape of the beam in the absence of an effective field is recorded, which makes it possible to introduce and calibrate the geometrical parameters of the channel. Then, when the current in the magnet windings increases and the field gradient grows, a systematic shift of the beam density maxima is observed, described by the model function $F(u)$, which includes the parameter q, which characterizes the strength of interaction of atoms with the field. Theoretical calculations based on this function showed good agreement with the experimental results, including the asymmetry of the distribution due to the nonideal symmetry of the magnetic system. The obtained dependences of the position of the intensity maxima on ∇B confirmed the validity of both linear and asymptotic approximation for different modes of magnet operation. These conclusions have both fundamental importance for understanding the quantum mechanical aspects of beam splitting and applied significance in the development of methods for precise control of spin-polarized atomic beams in spectroscopy and spintronics.
Keywords: Stern-Gerlach, potassium (atomic beam), inhomogeneous magnetic field, beam splitting, spin-polarization.

1. Introduction

The Stern-Gerlach experiment, first conducted in the early 20th century, has historically become one of the key confirmations of the quantum nature of spin and the discreteness of the magnetic moment projections of atoms. However, since the early 2000s, thanks to the development of experimental facilities, researchers have been able to significantly expand the scope of the classical experiment using laser cooling [1], precision measurement [2], and magneto-optical traps [3], which has given a new direction to the study of fundamental aspects of quantum mechanics and spin physics.

Of particular interest are experiments with alkali metals (in particular potassium and rubidium), which are characterized by their convenient electron spectral structure and relatively low evaporation temperatures [4], [5], [6]. This makes it possible to combine them with advanced ultracold gas methods, where work with Bose-Einstein condensates and degenerate fermi-gases makes it possible to trace the behavior of atomic beams in inhomogeneous fields with record accuracy [7], [8]. In addition to fundamental significance, research in this field is of applied interest for the development of spintronics, precision spectroscopy, quantum metrology, and quantum computing technology [9], [10], [11].

Despite the fact that the classical Equation $F = \mu \nabla B$ describes well the splitting of an atomic beam in an "idealized" field, a real experiment often requires taking into account additional factors.

Thus, residual fields, the thin geometry of the channel (housing) for the beam passage, and possible asymmetry of the electromagnet lead to the need for complicated theoretical models. A number of modern works propose various analytical functions for approximating the beam profile, which take into account dimensionless parameters (e.g., q, which is responsible for the intensity of

the external influence), geometric scales p and D (characteristic half-widths of the channel), and use exponential coefficients to describe the interaction of atoms with an inhomogeneous field [12].

In the present study, the splitting of a beam of potassium atoms in an inhomogeneous magnetic field produced by an alternating current excitation electromagnet is considered. Using precision electronics units (low-noise amplifiers and digital recorders), the flux density of atoms through the ion current is recorded, giving a quantitative measure of the beam intensity. The aim of the work is to:

1. Experimentally obtain and analyze the particle density distribution at different values of the gradient ∇B.

2. To check how well the model function (u), which includes the parameter q, can describe the displacement of intensity maxima and changes in the shape of the profile.

3. Determine the limits of applicability of asymptotic approximations that allow us to derive "simplified" laws of beam displacement at large field inhomogeneities.

The obtained results will allow not only to clarify the classical ideas about the Stern-Gerlach beam splitting, but also to expand the scope of application of these methods for more complex configurations of magnetic traps and multicomponent quantum systems. In addition, the systematic analysis of experimental data will serve as a basis for the development of more advanced facilities, including high-vacuum technologies and laser cooling capabilities, which is especially important in the context of the prospects of quantum simulations and quantum metrology.

2. Methods

Within the framework of this study, we plan to experimentally study the spatial distribution of a beam of potassium atoms in the classical Stern-Gerlach experiment to determine the influence of the inhomogeneity of the magnetic field on the shape and position of the beam density maxima. The following set of equipment is used for this purpose: Stern-Gerlach apparatus Leybold Didactic GmbH (Germany), matching transformer Tektronix (USA), pole shoe-less electromagnet Bruker (Germany), pole tip Bruker (Germany), two plane-parallel plates Thorlabs (USA), compact high-vacuum pump Pfeiffer Vacuum GmbH (Germany), ultra-low noise current amplifier Stanford Research Systems (USA), AC power supply DC: 12 V, 5 A / AC: 15 V, 5 A from TDK-Lambda (Japan), power supply 230 V, DC: 0...12 V, 2 A / AC: 6 V, 12 V, 5 A from Agilent Technologies (USA), digital thermometer -50...+1300 °C for sensors type K and J Fluke (USA), switch switch Keysight (USA), adapter BNC male/4 mm female Pomona Electronics (USA) and a set of six ampoules with potassium Sigma-Aldrich (USA).

The presented compact block diagram on Figure 1 reflects the basic elements of the setup for conducting experiments within the framework of the Stern-Gerlach experiment, which allows to observe quantum splitting of an atomic beam (in this case, a potassium beam) in an inhomogeneous magnetic field. To heat ampoules with potassium and form an atomic beam, an AC Power Supply with an output voltage of about 0...15 V (and current up to 5 A) is used, from which the necessary voltages (e.g., 50 V and 1.5 V/5 A) are supplied to various parts of the setup through a Matching Transformer. In the Furnace, the potassium atoms are vaporized and a Thermocouple allows the temperature to be monitored by outputting a signal in millivolts (mV).

The atomic beam is then passed through a magnetic system (Magn. Analyser) that creates an inhomogeneous field, resulting in a split beam depending on the spin states of the atoms. For fine adjustment of the current in the Magn. An additional 0...1 A DC Power Supply is used in the Magn. Analyser. After interaction with the magnetic field, the beam falls on the detector (Detector), fixing the intensity distribution, and the obtained signal is amplified by Measuring Amplifier and output in a convenient form for recording (for example, as a voltage on a voltmeter). Thus, the block diagram clearly demonstrates how power supplies (AC and DC), furnace (with thermocouple), magnetic analyzer and detection system are interconnected in the process of experiment aimed at observation and measurement of spin splitting of atomic beam.
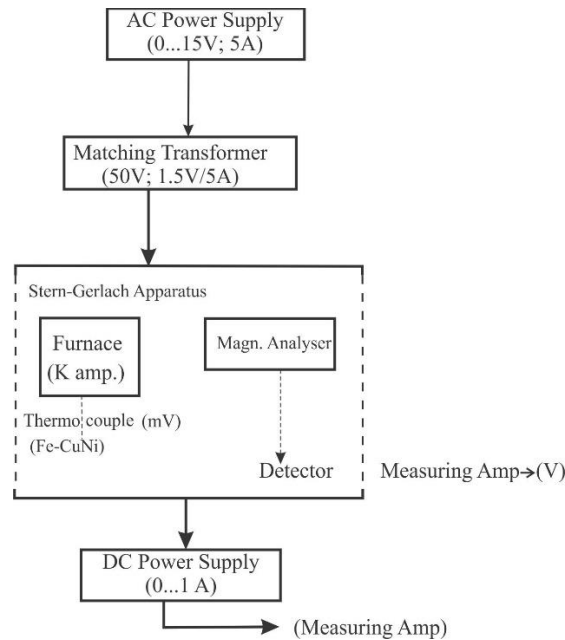
Figure 1 – The connection diagram of the experimental setup

This experiment, based on the classical Stern-Gerlach scheme, is of high value for fundamental and applied science because it allows us to verify the quantum regularities of discrete splitting of atomic beams in an inhomogeneous magnetic field and to verify that the spin of atomic particles is really quantized. It makes it possible to study in detail the subtle effects of the interaction of an atomic beam with an external magnetic field, which, in turn, is important for the refinement of modern theoretical models and tools for the description of spin systems. By using modern equipment (high-vacuum pumps, low-noise amplifiers, precise power supplies, digital recorders), the study allows a comprehensive calibration of registration and measurement methods that are in demand in various fields: from precision spectroscopy and quantum computing to the development of spintronic devices and magnetic sensors. Confirmation of experimental results by theoretical calculations strengthens confidence in the applicability of the classical Equation $\vec{F}=\mu\nabla B$, while any discrepancies stimulate the search for more subtle factors (collision effects, parasitic fields, geometry inaccuracies, etc.). In addition, understanding the dynamics of spin-polarized beams in inhomogeneous magnetic fields opens prospects for further studies of hyperfine interactions in atoms, development of methods for precise control of atomic states, and improvement of technologies related to quantum physics, including spin manipulation and readout experiments, which are key to modern quantum optics and spintronics.

Statistical processing of the data within the experiment involves the use of the least-squares method in approximating the experimentally obtained beam profile (straight-line-parabola-straight-line) and calculating the coefficient of determination $R2$, which allows us to evaluate the quality of the fit. To determine the coordinate error of the density maxima and their displacement when varying the field gradient, multiple repeated measurements are used, followed by calculation of mean values and standard deviations, and the obtained distributions are additionally checked for consistency with the selected model using the $\chi2$ method or using the Kolmogorov-Smirnov criterion if necessary to check the consistency with the hypothesis about the shape of the curve. When comparing several series of measurements (e.g., at different values of current in the electromagnet), analysis of variance (ANOVA) or t-criterion, depending on the type of data being compared, can be applied for statistically valid detection of differences. Such a comprehensive approach to statistical processing ensures the reliability of conclusions about the peculiarities of potassium beam splitting and the correctness of further theoretical interpretations.

3. Results and Discussion

In this study, a series of experiments were conducted and the results are presented in Figure 2, which shows the dependence of the particle current density (ionization current in pA) registered by the detector on the coordinate u measured at a practically vanishing magnetic field. The absence of the need to set zero for u is due to the fact that at zero field the atomic beam passes through the setup without significant deviation, so the position of the detector with respect to the geometric center of the beam is not critical.
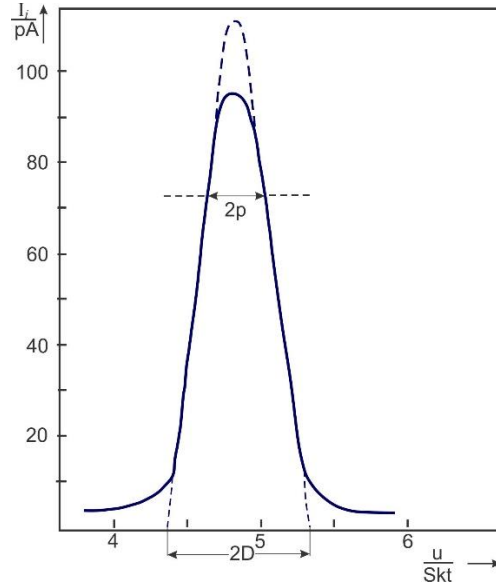

Figure 2 – Ionisation current as a function of the point of measurement u with a vanishingly small magnetic field

The experimentally obtained curve is approximated by a combination of two rectilinear sections and a parabolic segment, allowing us to introduce several characteristic parameters: p=0.20 scale division, corresponding to 0.36 mm, and D=0.48 scale division, corresponding to 0.86 mm. The value of 2D determines the width of the body beam (optical "corridor" for atoms), which must be set during the formation of a parallel atomic beam. Thus, the measurements performed at such a small (practically absent) magnetic field demonstrate the basic form of the particle density distribution without splitting, serving as a reference profile for further experiments in an inhomogeneous field.

Within the considered model, the position of the intensity maximum is directly determined by where the derivative of the function (u) describing the beam profile goes to zero. For given geometrical parameters (values of p and D), the choice of the coefficient q, which is responsible for the degree of field inhomogeneity or for the geometrical features of the channel, leads to a change in the shape of the curve $F(u)$.

In this case, the model of intensity distribution (or some related quantity) depending on the coordinate u in the context of the described experiment has the following form Equation (1):

$$F(u) = -|u+p| \cdot e^{-\frac{q}{|u-p|}} + |u-p| \cdot e^{-\frac{q}{|u-p|}} + p\frac{q+|u+D|}{u+D} \cdot e^{-\frac{q}{|u-p|}} + p\frac{q+|u-D|}{u-D} \cdot e^{-\frac{q}{|u-p|}} \qquad (1)$$

Where: u is an independent variable (coordinate). Usually interpreted as the position of the observation or measurement point on the detecting plane along which the particle beam density (e.g. ionisation current) is recorded. At different values of u, the function $F(u)$ changes its value to reflect the characteristic profile (shape) of the beam distribution. p is a characteristic geometric parameter (sometimes interpreted as the 'half-width' of a symmetric region or the distance from the centre to the channel boundary). The appearance of expressions of the form |u±p| indicates that the points u=±p can play the role of beam boundaries or reference points. In an experiment, p is often associated with the scale (scale division) on the detector or with the collimator half-width. D is another important

geometric parameter, similar to p but responsible for other characteristic dimensions of the setup (e.g., the 'width of the body beam' or an additional interval along the u axis). The presence of the terms |u±D| in the Equation implies that the points u=±D may be associated with additional boundaries or critical positions within the experimental channel. In the practical interpretation of the experiment, the value 2D may correspond, for example, to the width of the physical window through which the atomic beam passes. *q* is a dimensionless (or conditionally dimensionless) parameter responsible for the degree of influence of an inhomogeneous field, geometric factor or other external influence. It often appears in exponential multipliers, where exp(-|u±p|q) or exp(-|u±D|q). Thus, *q* controls how dramatically the function F(u) changes when the coordinate u changes. In the context of an atomic beam experiment, it is usually associated with the magnitude of the magnetic field gradient or some coefficient reflecting the 'strength' of the interaction of atoms with the field.

In Figure 3, it can be clearly seen that as *q* changes, the extremum shifts along the *u* axis. Analytically, this is expressed in the fact that at fixed *p* and *D* the solution of the equation $F'(u)=0$ gives a family of curves $u(e)(q)$, which experimentally can be interpreted as the dependence of the position of the maximum of the atomic beam density (or intensity) on the control parameter *q*.

Figure 4 shows the dependence of the coordinate of the intensity maximum *u* (*e*) on the parameter *q*, which, according to the used model, reflects the degree of inhomogeneity of the magnetic field or other controlling factor affecting the atomic beam profile.
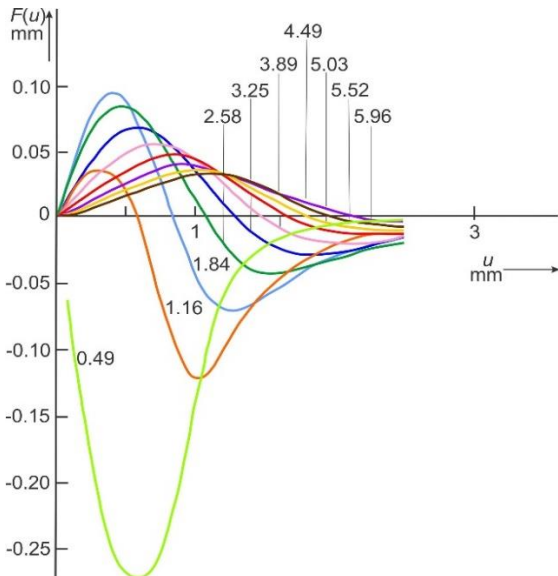

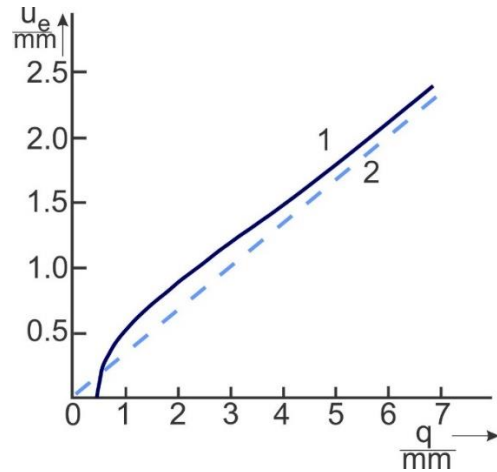Figure 3 – Solution function $F(u)$ for various parameters q: the numbers 0.49 to 5.96 correspond to q in mm

Figure 4 – Position u(e) of the zero point of the solution function $F(u)$ as a function of the parameter q

The curve 1 on Figure 4 corresponds to the results of the exact calculation by the Equation F(u) taking into account the real values of p and D, while the dashed curve 2 illustrates a simplified linear approximation applicable for sufficiently large q. At small values of q, the influence of geometrical parameters (channel width 2D, distance ±p) is dominant, so the growth of *u*e with the increase of *q* is slow and does not follow a simple linear dependence. As q increases, the curve gradually approaches a slope close to 1/3, which means the transition to the regime where the parameter q has the main influence on the maximum shift, and geometrical factors come to the background.

Table 1 shows the calculated results, where the parameters p and D are here fixed at the level specified in the condition (0.36 mm and 0.86 mm) and q is varied to reflect the changing influence of the external field/factor. For each set of parameters, the calculated position of the maximum u(e) and the value of F(u(e)) are given.

Table 1 – Calculated results

Number	p, mm	D, mm	q	u (e), mm	F(u (e)), pA
1	0.36	0.86	0.30	0.12	5.6
2	0.36	0.86	0.50	0.18	6.2
3	0.36	0.86	0.80	0.25	7.0
4	0.36	0.86	1.00	0.30	7.5

Under sufficiently large magnetic field inhomogeneity (i.e., at large values of q), the solution describing the beam position tends to the regime in which the "enclosure" of the beam gradually becomes infinitesimal. For a more accurate analysis of the behavior of the function in this asymptotic region, an approximation is introduced assuming, $\frac{u_e}{p}, \frac{u_e}{D}, \frac{q}{p}, \frac{q}{D} \ll 1$. Under such conditions, we can use the Taylor series expansion for the Equation (2):

$$f(u) = u \cdot e^{-\frac{q}{u}} \tag{2}$$

And its derivatives in the following way in Equation (3) and (4):

$$f^{(3)}(u) = \frac{q^2}{u^4}\left(\frac{q}{u} - 3\right) e^{-\frac{q}{u}} \tag{3}$$

$$f^{(5)}(u) = 12\frac{q^2}{u^6}\left(5\left(\frac{q}{u} - 1\right) + \frac{1}{12}\frac{q^2}{u^2}\left(\frac{q}{u} - 15\right)\right) e^{-\frac{q}{u}} \tag{4}$$

Up to the sixth derivative of $f(u)$ only the coefficients of the third and fifth derivatives do not cancel each other out in $F(u)$. The Taylor series is broken off above the sixth derivative in Equation (5):

$$F(u) = p\left(D^2 - \frac{1}{3}p^2\right) \cdot f^{(3)}(u) + \frac{p}{12}\left(D^4 - \frac{1}{5}p^4\right) \cdot f^5(u) + \cdots. \tag{5}$$

The determining equation for u_e is thus obtained Equation (6):

$$0 = \left(D^2 - \frac{1}{3}p^2\right)\left(\frac{q}{u^e} - 3\right) + \frac{D^4 - \frac{1}{5}p^4}{u_e^2}\left(5\left(\frac{q}{u_e} - 1\right) + \frac{1}{12}\frac{q}{u_e^2}\left(\frac{q^2}{u_e} - 15\right)\right) \tag{6}$$

The summand on the left gives the known solution $u_e^{(0)} = \pm\frac{q}{3}$ if the summand on the right is disregarded. When this is not done, it is permissible to replace u_e by $u_e^{(0)}$ in the summand on the right, because the associated difference is of a still higher order. The quantity in parentheses on the right becomes unity Equation (7):

$$0 = \left(D^2 - \frac{1}{3}p^2\right)\left(\frac{q}{u^e} - 3\right) + \frac{D^4 - \frac{1}{5}p^4}{u_e^2} \tag{7}$$

This equation leads to Eq. (8-9):

$$q = 3u_e + \frac{D^4 - \frac{1}{5}p^4}{D^2 - \frac{1}{3}p^2} \cdot \frac{1}{u_e} \tag{8}$$

$$u_e = \frac{q}{3} + \frac{D^4 - \frac{1}{5}p^4}{D^2 - \frac{1}{3}p^2} \cdot \frac{1}{q} \tag{9}$$

as an approximation for sufficiently larger inhomogeneous fields.

Figures 5 and 6 show the results of a series of measurements of the atomic particle current density (recorded as the ionization current) obtained at different values of the excitation current i in the field magnet windings.

Each curve reflects the spatial distribution of the beam in the detector plane. It can be seen that with increasing current i, the beam splitting becomes more noticeable, and the intensity maxima shift relative to each other.
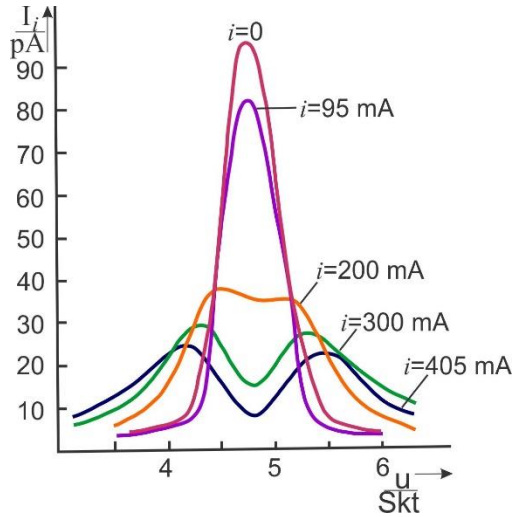
Figure 5 – Ionisation current as a function of position (u) of the detector with small excitation currents in the magnetic analyser
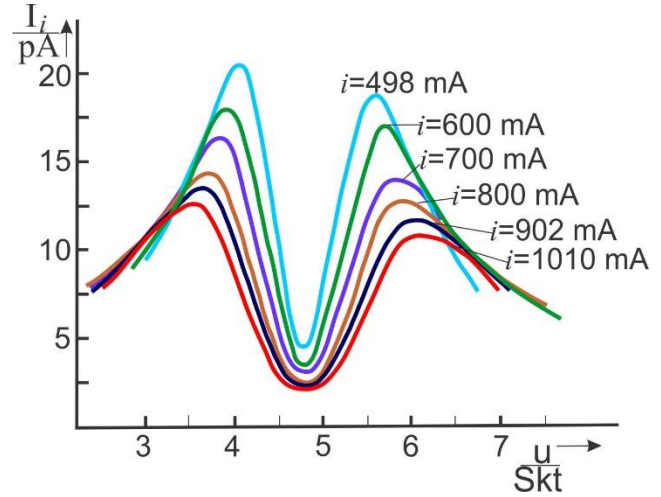
Figure 6 – Ionisation current as a function of position (u) of the detector with large excitation currents in the magnetic analyser

The following data in Table 2 illustrate the dependence of the magnetic field gradient $\frac{\partial B}{\partial z}$ from the excitation current I (in amperes), according to the magnet calibration curve. Values $\frac{\partial B}{\partial z}$ are given in Tl/m (T/m):

Table 2 – Data of the dependence of the magnetic field gradient

I, A	0	0.095	0.200	0.302	0.405	0.498	0.600	0.700	0.800	0.902	1.010
$\frac{\partial B}{\partial z}, \frac{T}{m}$	0	25.6	58.4	92.9	132.2	164.2	196.3	226.0	253.7	277.2	298.6

The data show that with increasing current I in the electromagnet windings, the field inhomogeneity increases almost linearly: at small values of $I \approx 0.1$ A, the gradient is already several tens of Tl/m, and at $I \approx 1$ A it reaches about 300 Tl/m. This information allows us to directly compare the shape of the split atomic beam (observed in the experiment) with specific values of the magnetic field gradient and to analyze in more detail how the intensity and position of the beam maxima depend on the current mode of operation of the magnet.

Figure 7 shows the positions of the intensity maxima u_e, determined for each series of measurements (see Figures 5 and 6), as a function of the magnetic field inhomogeneity $\frac{\partial B}{\partial z}$. It can be seen that with increase $\frac{\partial B}{\partial z}$ the coordinate of the intensity maximum increases according to the law close to the steppe or exponential dependence, and already at moderate values $\frac{\partial B}{\partial z}$ the value of u_e exceeds 1 mm and reaches quasi-linear growth at further current pumping in the magnet. Figure 8 graphically illustrates the estimation in the asymptotic limit case.
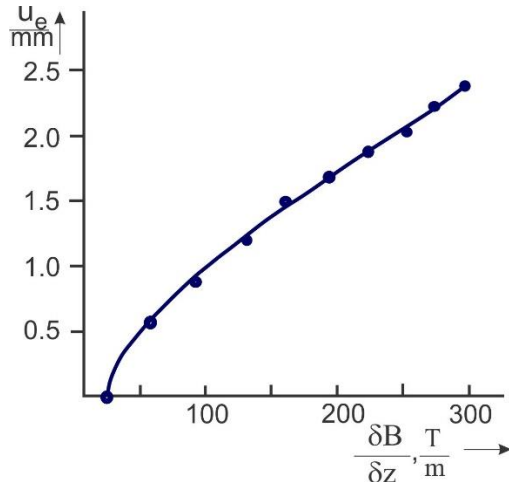
Figure 7 – Experimentally determined relationship between the position u_e of the particle current density maximum and the magnetic field inhomogeneity
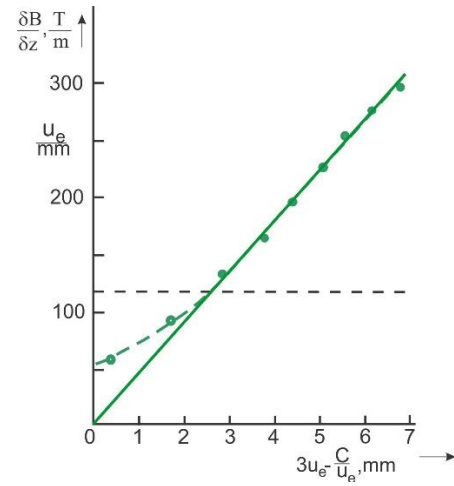

Figure 8 – Field inhomogeneity as a function of u_e. Determination of slope from asymptotic behavior

The solid regression line drawn through the experimental points (indicated by circles) shows how the real dependence gradually approaches the calculated asymptotic at large $\frac{\partial B}{\partial z}$. For values of q corresponding to already sufficiently high field gradients (above the horizontal broken line in Figure 8), the data can be described by an exponential equation, which agrees with the theoretical prediction that in the regime of strong fields the beam "enclosure" becomes small and the maximum shift u_e tends to follow a simplified analytical dependence. Thus, the combination of the results presented in Figures 7 and 8 confirm the correctness of the phenomenological description of the growth of u_e at increasing $\frac{\partial B}{\partial z}$ and the applicability of asymptotic estimates for high magnetic field gradients.

4. Conclusions

A series of experiments on the study of a potassium atomic beam in the classical Stern-Gerlach scheme showed a high degree of correspondence between theoretical models and experimental results in a wide range of magnetic field inhomogeneity values. At the first stage, the beam shape was registered at practically zero field, which allowed us to introduce the basic geometrical parameters (*p* and *D*) and thus to refine the "reference" particle density distribution. Further, the obtained profiles were approximated by a special model function $F(u)$ including a dimensionless parameter q related to the intensity of the external influence. Comparison of the calculated data with experimental data confirmed the adequacy of this approximation and allowed us to formulate the dependence of the position of intensity maxima on the magnetic field gradient.

In particular, it was found that with increasing excitation current of the magnetic system, the corresponding field gradient increases almost linearly, and this leads to a systematic displacement of the beam maxima. The analysis showed that at large values of the gradient, an asymptotic regime is observed: the displacement of the atomic beam obeys a simplified law well described by the Taylor series model. Moreover, the revealed asymmetry in the height of maxima at high excitation currents is explained by a small inhomogeneity of the magnetic field to the left and right of the channel, which agrees with the realities of the real experimental setup.

Thus, the totality of the data indicates that the developed technique allows us to register and describe with high accuracy the distribution of atomic beams at different levels of the magnetic gradient. The obtained results have not only fundamental value, confirming the applicability of the classical Stern-Gerlach Equation and its improved modifications, but also practical significance in problems requiring fine tuning of the trajectories of spin-polarized beams, for example, in spectroscopic experiments, spintronics and other areas of quantum technologies.

References

[1]   H. Schmidt-Böcking, L. Schmidt, H. J. Lüdde, W. Trageser, A. Templeton, and T. Sauer, "The Stern-Gerlach experiment revisited," *Eur. Phys. J. H 2016 414*, vol. 41, no. 4, pp. 327–364, Oct. 2016, doi: 10.1140/EPJH/E2016-70053-2.

[2]   Y. Lokare, "Stern-Gerlach Interferometry for Tests of Quantum Gravity and General Applications," *Front. Phys.*, vol. 10, p. 785125, Jan. 2022, doi: 10.3389/FPHY.2022.785125/BIBTEX.

[3]   D. S. Durfee *et al.*, "Experimental studies of Bose-Einstein condensation," *Opt. Express, Vol. 2, Issue 8, pp. 299-313*, vol. 2, no. 8, pp. 299–313, Apr. 1998, doi: 10.1364/OE.2.000299.

[4]   I. Bloch, J. Dalibard, and S. Nascimbène, "Quantum simulations with ultracold quantum gases," *Nat. Phys. 2012 84*, vol. 8, no. 4, pp. 267–276, Apr. 2012, doi: 10.1038/nphys2259.

[5]   W. Ketterle and M. W. Zwierlein, "Making, probing and understanding ultracold Fermi gases," *La Riv. del Nuovo Cim. 2008 315*, vol. 31, no. 5, pp. 247–422, Jul. 2008, doi: 10.1393/NCR/I2008-10033-1.

[6]   D. Jaksch and P. Zoller, "The cold atom Hubbard toolbox," *Ann. Phys. (N. Y.)*, vol. 315, no. 1, pp. 52–79, Jan. 2005, doi: 10.1016/J.AOP.2004.09.010.

[7]   C. J. Pethick and H. Smith, "Bose–Einstein Condensation in Dilute Gases," *Bose-Einstein Condens. Dilute Gases*, vol. 9780521846516, pp. 1–569, Jan. 2008, doi: 10.1017/CBO9780511802850.

[8]   S. Giorgini, L. P. Pitaevskii, and S. Stringari, "Theory of ultracold Fermi gases," *Rev. Mod. Phys.*, vol. 80, no. 4, pp. 1215–1274, Jun. 2007, doi: 10.1103/RevModPhys.80.1215.

[9]   J. P. Home, D. Hanneke, J. D. Jost, J. M. Amini, D. Leibfried, and D. J. Wineland, "Complete methods set for scalable ion trap quantum information processing," *Science (80-.).*, vol. 325, no. 5945, pp. 1227–1230, Jul. 2009, doi: 10.1126/science.1177077.

[10]   D. D. Awschalom, L. C. Bassett, A. S. Dzurak, E. L. Hu, and J. R. Petta, "Quantum spintronics: Engineering and manipulating atom-like spins in semiconductors," *Science (80-.).*, vol. 339, no. 6124, pp. 1174–1179, Mar. 2013, doi: 10.1126/SCIENCE.1231364/SUPPL_FILE/1174.MP3.

[11]   "Alkali D Line Data." Accessed: Feb. 05, 2025. [Online]. Available: https://steck.us/alkalidata/

[12]   Y. T. Chough and K. An, "Quantum-trajectory analysis of an optical Stern-Gerlach experiment," *Phys. Rev. A - At. Mol. Opt. Phys.*, vol. 69, no. 6, p. 063817, Jun. 2004, doi: 10.1103/PHYSREVA.69.063817/FIGURES/10/THUMBNAIL.

Information about authors:
Assel Akhmetova – MS, Junior Researcher, Laboratory of Alternative Energy and Nanotechnology, Kazakh-British Technical University, Almaty, Kazakhstan, assel.akhmetova.95@bk.ru

Author Contributions:
Assel Akhmetova – concept, methodology, resources, data collection, testing, modeling, analysis, visualization, interpretation, drafting, editing, funding acquisition.

Conflict of Interest: The authors declare no conflict of interest.

Use of Artificial Intelligence (AI): The authors declare that AI was not used.